Vol. 48 — N° 4 12 24 p. 887 – 908

GEOSTANDARDS and GEOANALYTICAL RESEARCH

Garnet Reference Materials for *In Situ* Lu-Hf Geochronology

Bruno V. **Ribeiro** (1, 2)*, Christopher L. **Kirkland** (1, 2), Matthijs **Smit** (3, 4), Kira **Musiyachenko** (3), Fawna J. **Korhonen** (5), Noreen J. **Evans** (6), Kai **Rankenburg** (6), Bradley J. **McDonald** (6), Stijn **Glorie** (7), Sarah E. **Gilbert** (8), Karsten **Goemann** (9), Ivan **Belousov** (10), Jeffrey **Oalmann** (10), Chris **Clark** (2) and Sean **Makin** (2)

(1) Timescales of Mineral Systems Group, School of Earth and Planetary Sciences, Curtin University, Perth, WA 6102, Australia
(2) School of Earth and Planetary Sciences, Curtin University, Perth, WA 6102, Australia
(3) Department of Earth, Ocean and Atmospheric Sciences, University of British Columbia, Vancouver, British Columbia, Canada
(4) Department of Geosciences, Swedish Museum of Natural History, Stockholm, Sweden
(5) Geological Survey of Western Australia, 100 Plain Street, East Perth, WA 6004, Australia
(6) John de Laeter Centre, Curtin University, Perth, WA, Australia
(7) Department of Earth Science, School of Physical Sciences, University of Adelaide, Adelaide, South Australia, Australia
(8) Adelaide Microscopy, University of Adelaide, South Australia, Australia
(9) Central Science Laboratory, University of Tasmania, Hobart, Australia
(10) CODES Analytical Laboratories, University of Tasmania, Hobart, Australia
* Corresponding author. e-mail: bruno.vieiraribeiro@curtin.edu.au

In situ **garnet Lu-Hf geochronology has the potential to revolutionise the chronology of petrological and tectonic processes, yet there is a paucity of well-characterised reference materials to account for laser-induced matrix-dependant elemental fractionation. Here, we characterise two reference garnets GWA-1 (Lu ~ 7.0 µg g^{-1}) and GWA-2 (Lu ~ 8.5 µg g^{-1}) for *in situ garnet* Lu-Hf geochronology. Isochron ages from isotope dilution Lu-Hf analyses yield crystallisation ages of 1267.0 ± 3.0 Ma with initial $^{176}Hf/^{177}Hf_i$ of 0.281415 ± 0.000012 (GWA-1), and 934.7 ± 1.4 Ma with $^{176}Hf/^{177}Hf_i$ of 0.281386 ± 0.000013 (GWA-2). *In situ* Lu-Hf analyses yield inverse isochron ages up to 10% older than the known crystallisation age due to matrix effects between garnet and reference glass (NIST SRM 610) under different instrument tuning conditions. This apparent age offset is reproducible for both materials within the same session and can be readily corrected to obtain accurate ages. Our results demonstrate that GWA-1 and GWA-2 are robust reference materials that can be used to correct for matrix-analytical effects and also to assess the accuracy of *in situ* Lu-Hf garnet analyses across a range of commonly encountered garnet compositions.**

Keywords: *in situ* Lu-Hf geochronology, garnet geochronology, garnet reference material, LA-ICP-MS/MS, garnet isotope geochemistry.

Received 21 Feb 24 – Accepted 01 Jul 24

Deciphering the Earth's tectonic evolution has been a repeated goal in Earth science as it connects the lithosphere to the atmosphere, hydrosphere and biosphere (Cawood *et al.* 2013, 2022, Cawood 2020, Mulder *et al.* 2021, Spencer 2022, Spencer *et al.* 2022). When approaching this challenge, quantifying the pressure-temperature-time (*P-T-t*) history of metamorphic rocks is critical for reconciling thermal regimes throughout deep time (Brown and Johnson 2018, Holder *et al.* 2019, Cawood 2020, Palin *et al.* 2020).

Garnet is of major relevance due to its ability to faithfully track *P-T-t* conditions in its major and trace element composition, and Sm-Nd, Lu-Hf and U-Pb isotopic systems (Pollington and Baxter 2010, Baxter and Scherer 2013, Smit *et al.* 2013, 2014, Baxter *et al.* 2017, Millonig *et al.* 2020, Tamblyn *et al.* 2021, Ribeiro *et al.* 2022, 2023, Simpson *et al.* 2023, Kaempf *et al.* 2024, Shu *et al.* 2024). Garnet Sm-Nd and Lu-Hf geochronology has been widely deployed to address tectono-metamorphic questions for decades, commonly through isotope dilution (ID) analysis, requiring garnet selection, digestion, and isotope separation via ion-exchange chromatography. Such techniques offer high analytical precision at the expense of time-consuming laboratory processes, and this approach may lead to mixed ages in cases of polymetamorphic garnets

doi: 10.1111/ggr.12579

recording multiple growth stages. Microdrilling specific garnet zones is an effective approach to avoid mixed textural domains (Pollington and Baxter 2010, Tual *et al.* 2022), yet this labour-intensive method typically requires cm-sized garnet grains that may not be present across all samples of interest. *In situ* garnet geochronology via laser ablation-inductively coupled plasma-mass spectrometry (LA-ICP-MS) provides a rapid, spatially resolved alternative to conventional garnet geochronology that has been developed for the U-Pb and Lu-Hf systems (Seman *et al.* 2017, Millonig *et al.* 2020, Simpson *et al.* 2021, Wu *et al.* 2023, Shu *et al.* 2024). These rapid techniques open new possibilities for the investigation of *P-T-t* conditions leading to garnet growth (Tamblyn *et al.* 2021, Ribeiro *et al.* 2022, 2023, Gaidies *et al.* 2023, Simpson *et al.* 2023).

In situ measurement of Lu-Hf in garnet has become a key technique to resolve the timing of garnet formation and tectonic processes, however we note the lack of characterised reference materials (RMs; i.e., garnet with well-defined reference ages determined by isotope dilution Lu-Hf analysis) that are required to evaluate data quality and analytical factors such as matrix-dependence, long-term reproducibility, and uncertainty on isochron ages. Some of the most commonly used have inferred ages from other minerals and chronometers (e.g., Högsbo garnet, Simpson *et al.* 2021), or from multi-session Lu-Hf isochron dates (Glorie *et al.* 2024). Developing well-characterised garnet RMs would advance *in situ* Lu-Hf garnet geochronology, bolstering a technique that may greatly enhance our ability to better constrain tectonometamorphic processes.

In this paper, we introduce two new garnet reference materials (GWA-1 and GWA-2) for *in situ* Lu-Hf geochronology via LA-ICP-MS/MS. We provide detailed microstructural, chemical and isotopic characterisation of both RMs. *In situ* garnet Lu-Hf isotopic data were obtained in two laboratories and compared with isotopic data obtained through conventional solution ID Lu-Hf analysis via multi-collector coupled plasma-mass spectrometry (MC-ICP-MS), providing the crystallisation age of each material. The materials comprise metamorphic garnet from a Mesoproterozoic psammitic gneiss in the Albany-Fraser Orogen (south-eastern Western Australia; GWA-1) and igneous garnet from a Neoproterozoic pegmatite in the Capricorn Orogen (northern Western Australia; GWA-2).

Sample context

The garnet materials analysed in this study are from two legacy samples held in the collection of the Geological Survey of Western Australia's (GSWA), including a pegmatite (GSWA 190667, Wingate *et al.* 2011) and a psammitic gneiss (GSWA 182431, Wingate *et al.* 2016). Zircon U-Pb isotopes measured via sensitive high-resolution ion microprobe of these rock samples are available in the GSWA's electronic portal GeoView.WA (https://geoview.dmp.wa.gov.au/geoview/?Viewer=GeoView). Hereafter, garnet from the psammitic gneiss (GSWA182431) will be referred as GWA-1, and those from the pegmatite (GSWA190667) as GWA-2.

The psammitic gneiss (GWA-1) was sampled from the Gwynne Creek Gneiss, Arid Basin, which occurs in the northeastern part of the Albany Fraser Orogen (southeast Western Australia, Figure 1). The Gwynne Creek Gneiss is well exposed along the creek, and is dominated by psammitic and pelitic gneiss (Spaggiari *et al.* 2014). The rock is a medium-grained and quartz rich paragneiss with layering 10–30 cm thick (Figure 2a). It is interbedded withmedium-grained semi-pelitic gneiss that includes thin layer-parallel leucosomes and biotite-rich layers locally with garnet and pegmatite veins (Wingate *et al.* 2016). The rock is composed of plagioclase, quartz, garnet (3–4% by volume), biotite and hornblende, with minor andalusite, apatite, titanite, zircon and opaque phases. Garnet grains are up to 2–3 mm in diameter, euhedral to subhedral, and dispersed throughout the rock together with epidote, biotite and ± hornblende. Zircon in the sample is characterised by 1681–1450 Ma detrital cores and metamorphic zircon rims with low Th/U ratios (median of 0.01), yielding a weighted mean $^{207}Pb/^{206}Pb$ age of 1299 ± 8 Ma (N = 10, MSWD = 0.7; Figure 2b) (Wingate *et al.* 2016).

The pegmatite (GWA-2) was sampled from a rare earth element-bearing granite pegmatite, which is part of the Thirty-Three Supersuite, Gascoyne Province, Capricorn Orogen (northern Western Australia, Figure 1) (Wingate *et al.* 2011). The Thirty-Three Supersuite comprises ~420 km^2 of leucocratic granite plutons and pegmatites localised at the central part of the Gascoyne Province (Piechocka *et al.* 2017). The rock is composed of quartz, muscovite, lepidolite, ± garnet (~3–4% by volume), and locally contains tourmaline with feldspar megacrysts (Figure 2c). Garnet grains are up to 4 mm in diameter, euhedral, and generally associated with mica aggregates including muscovite and lepidolite (Wingate *et al.* 2011). Zircon U-Pb ages revealed a xenocryst component spanning 2522–1700 Ma. Magmatic zircon grains define a weighted mean $^{207}Pb/^{206}Pb$ age of 938 ± 4 Ma (N = 15, MSWD = 1.5; Figure 2d) (Wingate *et al.* 2011).

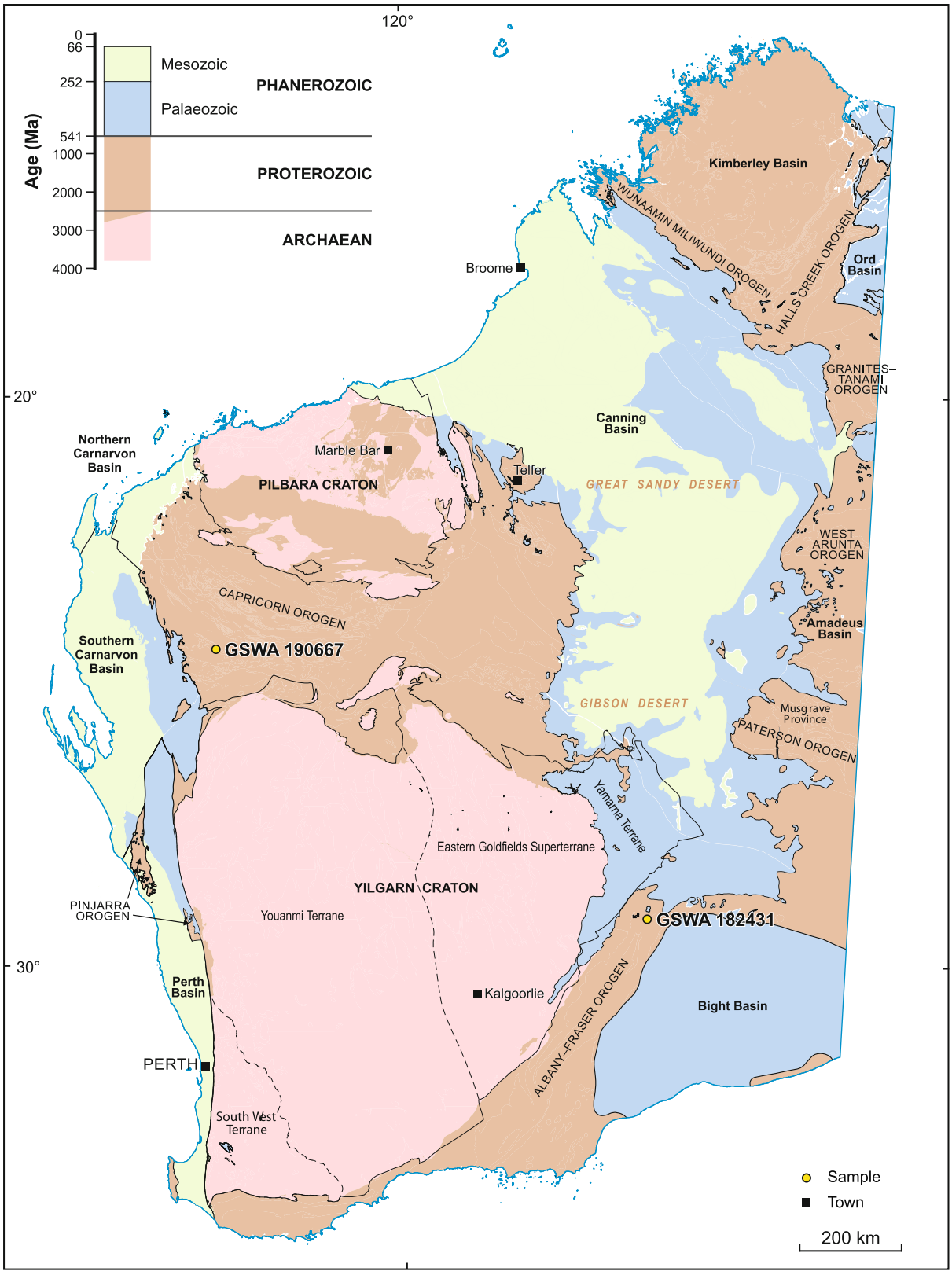

Figure 1. Simplified tectonic map of Western Australia (adapted from GSWA 2022) indicating the location of samples GSWA 182431 (GWA-1; -29.4088, 124.9479) and GSWA 190667 (GWA-2; -24.6296, 116.3652).

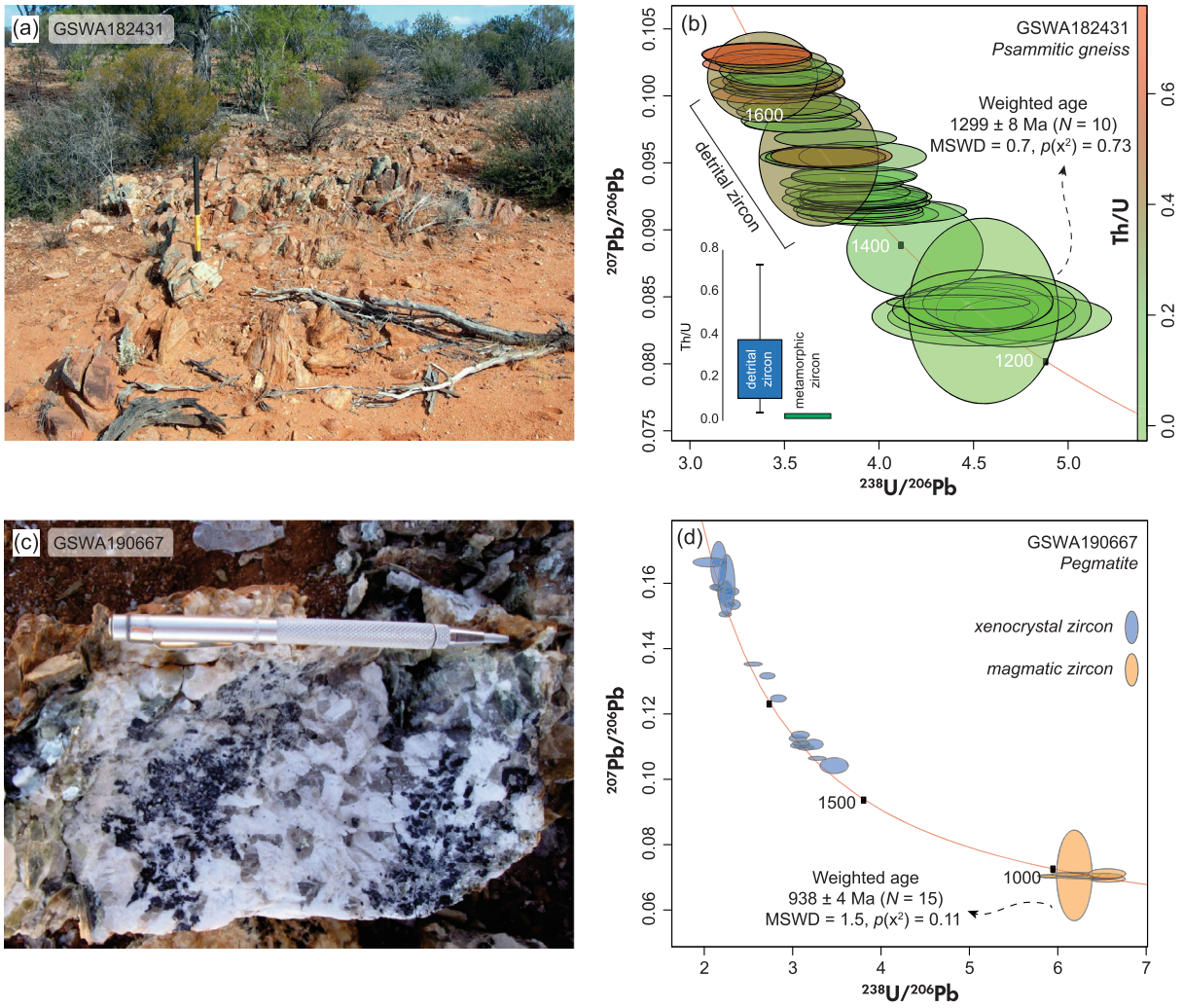

Figure 2. Field photographs and zircon U-Pb dates of samples GSWA182431 (a, b; adapted from Wingate *et al.* 2016) and GSWA190667 (c, d; adapted from Wingate *et al.* 2011). Uncertainties are stated at the 2*s* level of confidence. Weighted means for samples GSWA182431 and GSWA190667 were calculated using the $^{206}Pb/^{238}U$ and $^{207}Pb/^{206}Pb$ ages, respectively.

Methods

Garnet from both samples were microstructurally, chemically, and isotopically characterised using an array of high-spatial resolution techniques. Internal microstructures were assessed through electron backscatter diffraction (EBSD) mapping. Major element composition was quantified via X-ray elemental mapping, and also spot analysis using an electron probe microanalyser (EPMA). Spatial variation of trace elements was investigated through LA-ICP-MS mapping. Garnet Lu-Hf isotopes were obtained via solution ID MC-ICP-MS and *in situ* LA-ICP-MS/MS. The *in situ* chemical and isotopic techniques were employed on polished rock pieces mounted in 1-inch epoxy round mounts.

Microstructural analysis

Crystal-plastic deformation may affect trace element and isotope mobility (Reddy *et al.* 2007, 2009, Timms *et al.* 2011, Papapavlou *et al.* 2017, Ribeiro *et al.* 2020, Gordon *et al.* 2021). Accordingly, the garnet grains were subjected to electron backscatter diffraction EBSD analysis. The EBSD data were collected with a TESCAN Clara field emission scanning electron microscope (coupled to an Oxford Symmetry EBs detector) at the John de Laeter Centre, Curtin University, Australia. The samples were polished on a Buehler VibroMet II for 4 h using a 0.05-µm colloidal silica solution prior to data collection. A thin carbon coat was applied to mitigate charging (~ 2.5 µm thickness). Analytical conditions included 20 kV acceleration voltage, 1 nA beam current, 20 mm working distance, 70°

sample tilt, 30 ms exposure time and 3 μm step-size. EBSD data were processed using AZtecCrystal v2.1.

Garnet chemistry

Two garnet grains from each sample were selected for spot chemical analysis, and one garnet grain per sample was chosen for detailed X-ray elemental mapping in order to identify potential chemical zoning. Major element data were acquired at the Central Science Laboratory, University of Tasmania, on a JEOL JXA-8530F Plus field-emission electron probe microanalyser with five wavelength dispersive spectrometers, which operated at an accelerating voltage of 15 kV, beam current of 30 nA and beam diameter of 2 μm. The calibration set-up included analysing crystals LIFL for Mn and Fe, PETL for Ca and Ti, TAPL for Na and Mg, and TAP for Al and Si, with *Kα* lines being used for all elements. The major elements were calibrated against natural and synthetic RMs such as synthetic rutile for Ti, natural rhodonite for Mn, natural jadeite for Na (all P&H Developments, UK), Hematite Harvard H92649 for Fe, Plagioclase Lake County NMNH115900 for Al, wollastonite (UTas in house) for Ca, and Olivine MongOL Sh11-2 for Mg and Si.

Peak and background counting times were 10 s for Na, 20 s for Si, Ca and Ti, 30 s for Al and Mg, and 60 s for Mn and Fe. The background correction method was linear off-peak for Al, Ca, and Fe, and exponential for Si, Mg, Ti, Mn, and Na. Unknown and reference material intensities were corrected for dead time. The matrix correction method was PAP with the LINEMU mass absorption coefficient dataset. Garnet structural formulae were calculated using MinPlot (Walters 2022) using 12-equivalent oxygens.

X-ray elemental maps were acquired with the same spectrometer settings as described above by stage scanning at a dwell time of 50 ms per pixel with a beam current of 80 nA and beam diameter of 2 μm. Peak intensity maps were acquired and the mean atomic number method with calibration curves acquired on reference materials was used for background correction. The RMs described above were used for map quantification. Background-corrected X-ray elemental maps were produced using the XMapTools platform (Lanari *et al.* 2014). The complete chemical dataset is presented in online supporting information Appendix S1.

Trace element mapping

Garnet trace element mapping was performed via LA-ICP-MS at CODES Analytical Laboratories facility, University of Tasmania. The analyses were conducted on a RESOLution 193 nm SE excimer laser ablation system connected to an Agilent 7900 quadrupole mass spectrometer. The sample ablation was performed in He atmosphere flowing (at 0.35 l min^{-1}) and combined with Ar carrier gas (at 1.05 l min^{-1}) after ablation. The entire grain area was covered by a raster of parallel ablation lines. A square laser beam of 12 μm was used with a 12 μm s^{-1} rastering speed. The following isotopes were measured: ^{23}Na, ^{24}Mg, ^{27}Al, ^{29}Si, ^{31}P, ^{43}Ca, ^{45}Sc, ^{49}Ti, ^{51}V, ^{53}Cr, ^{55}Mn, ^{57}Fe, ^{66}Zn, ^{69}Ga, ^{89}Y, ^{90}Zr, ^{118}Sn, ^{139}La, ^{140}Ce, ^{146}Nd, ^{147}Sm, ^{153}Eu, ^{157}Gd, ^{163}Dy, ^{172}Yb, ^{175}Lu, ^{178}Hf, ^{208}Pb, ^{232}Th and ^{238}U. Total sweep time was equal to 0.39 s with dwell times for individual masses varying between 2 ms for major elements and 20 ms for Lu and Hf. Ablation was carried out using a laser frequency of 10 Hz and laser fluence of approximately 3.5 J cm^{-2}. NIST SRM 612 was used as the primary RM for initial quantification and instrument drift correction, and *Gs*-1G and BCR-2G were used as secondary RMs. Quantification was performed using ^{27}Al as the internal standard element, and normalising all measured cations to 100% *m/m* oxide total. The LADR software (Norris and Danyushevsky 2018) was used to determine conversion factors with final image processing done with an in-house developed Python script. Trace element maps were constructed using the XMapTools platform (Lanari *et al.* 2014).

Isotope dilution Lu-Hf geochronology

In order for a material to be considered as a certified and well-characterised reference material, state-of-the-art techniques need to be employed to establish its chemical, isotopic and physical properties (May *et al.* 2000). In the geochronology field, determining the age of such reference materials is essential, as it provides a baseline for the isotopic measurements of additional reference materials and unknowns (samples). Similar to zircon U-Pb reference materials (e.g., Wiedenbeck *et al.* 1995, Slama *et al.* 2008), the determination of garnet reference Lu-Hf ages requires isotope dilution techniques such as isotope separation via chromatography (Münker *et al.* 2001, Sprung *et al.* 2010) and isotopic measurement via MC-ICP-MS (e.g., Scherer *et al.* 2001, Baxter and Scherer 2013, Smit *et al.* 2013, Baxter *et al.* 2017). In this study, we employed such techniques to determine the reference Lu-Hf ages of GWA-1 and GWA-2, essential to further evaluate the garnet Lu-Hf isotopic data collected via LA-ICP-MS/MS.

Whole rock and three garnet aliquots of GWA-1 and GWA-2 were selected for solution ID Lu-Hf geochronology to constrain the crystallisation ages of the potential

reference garnets. The samples were analysed at the Pacific Centre for Isotopic and Geochemical Research, Department of Earth, Ocean, and Atmospheric Sciences, The University of British Columbia. Garnet fractions and whole-rock powders were transferred to 15-ml screw-top PFA vials. The garnet grains were washed twice with de-ionised water, bathed in 1 mol l^{-1} HCl at room temperature for 1 h, rinsed again and mixed with a high-Lu/Hf ^{176}Lu-^{180}Hf tracer. Garnet samples were digested through repeated addition of concentrated HF, HNO_3 and $HClO_4$, and 6-mol l^{-1} HCl, each step followed by evaporation to dryness. The powders were mixed with a low-Lu/Hf ^{176}Lu-^{180}Hf tracer and were digested by the same procedure in an attempt to avoid co-dissolution of zircon that may sequester inherited Hf. After digestion, all samples were dried, re-dissolved in 6 mol l^{-1} HCl, diluted to 3 mol l^{-1} HCl using de-ionised H_2O, and centrifuged in 10-ml polypropylene tubes. The centrifuged solutions were separated from any undigested residue and were loaded onto polypropylene columns containing a 1 ml of BioRad© Ln resin bed and subjected to REE-HFSE (rare earth element-high field-strength element) separation chromatography following the procedures of Münker *et al.* (2001) and Sprung *et al.* (2010). The Lu and Hf isotope analyses were undertaken with a Nu Instruments Plasma I multi-collector ICP-MS instrument. For Lu determinations, isobaric interference of ^{176}Yb on ^{176}Lu was corrected using an exponential ^{176}Yb/^{171}Yb–^{174}Yb/^{171}Yb relationship as calibrated through replicate analyses of NIST SRM Yb solution standards (Blichert-Toft *et al.* 2002). Instrumental mass bias was assumed to follow an exponential law and was corrected applying ^{179}Hf/^{177}Hf = 0.7325 and ^{173}Yb/^{171}Yb = 1.1296 (Vervoort *et al.* 2004). The isobaric interferences of ^{180}Ta and ^{180}W on ^{180}Hf were corrected by measuring ^{181}Ta/^{177}Hf and ^{183}W/^{177}Hf, and applying mass bias based on ^{179}Hf/^{177}Hf. Instrumental drift was corrected by assuming linear time dependence. The ^{176}Hf/^{177}Hf values are reported relative to those of ATI-475, an in-house-developed Hf isotope RM that was made from the original Hf metal ingots from which the international reference solution JMC-475 was produced (^{176}Hf/^{177}Hf = 0.282160, Vervoort and Blichert-Toft 1999). Replicate analyses of ATI-475 at mass fractions bracketing that of samples showed ^{176}Hf/^{177}Hf "external reproducibility" to be 25 μg g^{-1} or better during the course of our measurement session. Total procedural Hf blanks were consistently below 10 pg. Lu-Hf isochron ages were calculated using IsoplotR (Vermeesch 2018) using the ^{176}Lu decay constant of Scherer *et al.* (2001) and Söderlund *et al.* (2004). All uncertainties are presented at 2 standard deviation (2*s*) level. The ID Lu-Hf isotopic data are presented in Table 2.

In situ Lu-Hf geochronology

Curtin University: *In situ* Lu-Hf geochronology was performed at the John de Laeter Centre GeoHistory Facility, Curtin University, Australia. Data collection was performed across three measurement sessions, which are specified in the dataset presented in Appendix S2. *In situ* Lu-Hf measurements were carried out on garnet GWA-1 and GWA-2 grains mounted in 1-inch^2 polished epoxy mounts.

The analytical set-up involved a RESOlution 193 nm ArF excimer laser with a Laurin Technic S155 sample cell coupled to an Agilent 8900 triple quadrupole ICP-MS/MS using NH_3/He reaction gas in the reaction cell (20% NH_3 in He pre-mixed gas). This configuration enabled measurement of Lu and Hf isotopes following the approach of Simpson *et al.* (2021). The laser, gas flow and mass spectrometer set-up are summarised in Table 1. A 'squid' mixing device (Laurin Technic) was used to smooth the aerosol pulses between the laser and mass spectrometer. Garnet samples were ablated using a fluence of ~ 3.5 J cm^{-2}, repetition rate of 10 Hz and a circular laser beam of 130 μm (sessions one and two) and 193 μm (session three). A low flow of N_2 (4 ml min^{-1}) was added to the carrier gas before the ICP torch to enhance sensitivity (Hu *et al.* 2008). Instrument tuning was performed using NIST SRM 610 glass in single quadrupole (no-gas mode) to optimise plasma conditions, minimise oxide interferences and maximise ^{175}Lu sensitivity using circular laser beam of 64 μm (sessions one and two) and 50 μm (session three). After shifting to MS/MS mode, the ICP-MS was tuned for maximise sensitivity for Hf reaction products using NH_3/He before each session. In order to test the importance of flushing the reaction cell with high NH_3/He flow rate prior to tuning and analysis, we tested three set-ups to evaluate the Hf conversion rate and instrument sensitivity. Session one was conducted without reaction cell flushing prior to analysis. Session two and three were carried out after flushing the reaction cell with the reaction gas (20% NH_3 in He pre-mixed gas) with a high flow rate (> 95% in the mass flow controller) for 0.5 and 2.0 h, respectively.

Data reduction was performed in Iolite 4 (Paton *et al.* 2011) using an in-house data reduction scheme after Ribeiro *et al.* (2023). The NIST SRM 610 glass was used as the primary RM with assumed ^{176}Lu/^{177}Hf and ^{176}Hf/^{177}Hf compositions of 0.1379 ± 0.0050 and 0.282122 ± 0.000009 (Nebel *et al.* 2009; all uncertainties quoted as 2*s*). The following isotopes were measured ('+' refers to mass-shifted isotopes), with dwell times in milliseconds (ms) between brackets: ^{27}Al (5), ^{43}Ca (5), ^{47}Ti (5), ^{89}Y (5), ^{90}Zr (5), ^{140}Ce (5), ^{172}Yb (10), $^{172+82}$Yb (30), ^{175}Lu (10), $^{175+82}$Lu (10), $^{176+82}$Hf (150) and $^{178+82}$Hf (150).

Table 1.
Analytical conditions for *in situ* garnet Lu-Hf via LA-ICP-MS/MS at the GeoHistory Lab (Curtin University) and at Adelaide Microscopy (University of Adelaide)

	Curtin University			University of Adelaide
Laser ablation system	**Session 1**	**Session 2**	**Session 3**	**Session 1**
Ablation cell	RESOlution-LR ArF excimer laser			RESOlution-LR ArF excimer laser
Laser wavelength (nm)	193			193
Pulse width (ns)	20			20
He flow rate (l min^{-1})	320			350
N_2 flow rate (ml min^{-1})	4			4
Fluence (J cm^{-2})	3.5			3.5
Repetition rate (Hz)	10			10
Ablation duration (s)	40			40
Background duration (s)	40			30
Laser beam diameter (µm)	50 and 64 - NIST SRM 610/612 130 and 193 - Garnet			30 and 67 - NIST SRM 610/612 43 and 100 (Högsbo), 173 (Garnets)
Sampling mode	Static spot ablation			Static spot ablation
Plasma				
RF power (W)	1500	1500	1500	1350
Sampling depth (mm)	5.0	4.7	5.0	4.5
Nebuliser gas (Ar, l min^{-1})	1.0	1.0	1.0	1.0
Lenses				
Extract 1 (V)	-17.0	-18.0	-25.1	-6.0
Extract 2 (V)	-250.0	-250.0	-250.0	-170.0
Omega bias (V)	-150.0	-150.0	-130.0	-105.0
Omega lens (V)	6.0	7.0	9.9	10.0
Q1 entrance (V)	-50.0	-25.0	4.0	-15.0
Q1 exit (V)	0.0	0.0	1.0	-5.0
Cell focus (V)	2.0	1.9	1.9	-2.0
Cell entrance (V)	-110.0	-100.0	-128.0	-130.0
Cell exit (V)	-70.0	-70.0	-75.0	-80.0
Deflect (V)	6.5	6.8	6.5	6.0
Plate bias (V)	-60.0	-63.0	-55.0	-80.0
Q1				
Q1 bias (V)	0.0	-0.1	-0.1	-1.0
Q1 pre-filter bias (V)	-10.0	-10.0	-10.0	-10.0
Q1 post-filter bias (V)	-10.0	-10.0	-10.0	-10.0
Collision cell				
He flow rate (ml min^{-1})	1.0	1.0	1.0	1.0
3rd gas (NH_3) flow rate (%)	20*	20*	20*	30**
OctP bias (V)	-3.0	-3.1	-2.0	-5.0
Axial acceleration (V)	2.0	2.0	2.0	2.0
OctP RF (V)	180	180	180	180
Energy discrimination (V)	-7.0	-20.0	-13	-15
Wait time offset (ms)	2	2	2	2

Symbols: *NH_3 supplied as 20% NH_3 in He (Curtin University); **NH_3 supplied as 10% NH_3 in He (University of Adelaide).

The Lu-Hf isochron ages were calculated using the inverse isochron regression (Li and Vermeesch 2021) in IsoplotR (Vermeesch 2018) with ^{176}Lu decay constant after Scherer *et al.* (2001) and Söderlund *et al.* (2004). Inverse isochron ages and analytical uncertainties are stated at the 2*s* level of confidence (95% confidence). NIST SRM 612 glass was used as a secondary RM to evaluate the accuracy of the $^{176}Lu/^{177}Hf$ and $^{176}Hf/^{177}Hf$ measurement results, which returned $^{176}Lu/^{177}Hf$ of 0.1390 ± 0.0030 (N = 49, mean ± 2SE) and $^{176}Hf/^{177}Hf$ of 0.2819 ± 0.0009 (N = 49, 2*s*). These results agree within uncertainty with the reference values of 0.1346 ± 0.0033 and 0.282100 ± 0.000038 (Nebel *et al.* 2009).

Table 2.
Solution ID Lu-Hf chemical and isotopic data for GWA-1 and GWA-2

Aliquot	Lu (μg g^{-1})	Hf (μg g^{-1})	^{176}Lu/^{177}Hf	2*s* (abs)	^{176}Hf/^{177}Hf	2*s* (abs)
Garnet GWA-1						
Gt-1	7.75	1.03	1.069000	0.003000	0.307037	0.000015
Gt-2	7.06	2.98	0.335800	0.000800	0.289438	0.000013
Gt-3	6.09	1.37	0.630100	0.001600	0.296499	0.000016
WR-1	1.00	1.35	0.105300	0.000300	0.283940	0.000012
Garnet GWA-2						
Gt-1	8.56	0.22	5.504000	0.014000	0.378136	0.000022
Gt-2	8.68	0.22	5.577000	0.014000	0.379527	0.000024
Gt-3	8.48	0.35	3.461000	0.009000	0.342425	0.000018
WR-1	0.35	1.69	0.029160	0.000070	0.281899	0.000013

Uncertainties are presented at 2 standard deviation (absolute value; abs). Gt and WR refer respectively to garnet and whole-rock aliquots.

University of Adelaide: *In situ* Lu-Hf geochronology was conducted in a single measurement session at Adelaide Microscopy, The University of Adelaide, Australia, using mounted garnet GWA-1 and GWA-2 grains in polished epoxy mounts. The analyses were carried out using an identical hardware set-up as above: RESOlution-LR 193 nm ArF excimer laser ablation system, connected to an Agilent 8900 triple quadrupole ICP-MS/MS via a squid mixing device. Analytical conditions followed Simpson *et al.* (2021) and Glorie *et al.* (2024), using NH_3/He as the reaction gas (10% NH_3 in He pre-mixed gas). The NH_3/He gas line was flushed at a high flow rate for several hours prior to tuning and analysis. The garnet samples were ablated using a fluence of approximately 3.5 J cm^{-2}, repetition rate of 10 Hz, and a circular laser beam of 173 μm. A low flow of N_2 (4 ml min^{-1}) was added to the carrier gas before the ICP torch to enhance sensitivity (Hu *et al.* 2008). NIST SRM 610 was used as the primary RM for ^{175}Lu/^{176}Hf and ^{178}Hf/^{176}Hf ratio calibrations (Nebel *et al.* 2009) and was analysed at two spot sizes (30 μm and 67 μm) to measure ^{175}Lu in both pulse and analogue detector modes (Glorie *et al.* 2024). The cross-over count rate (i.e., pulse limit × PA factor) for ^{175}Lu was 4.81 × 10^6 counts per second (cps) in this measurement session. Additional laser, gas flow and mass spectrometer settings are summarised in Table 1.

All data were processed in LADR (Norris and Danyushevsky 2018) using a customised data reduction workflow that calculates error correlations from the raw isotopic ratios for each analytical sweep. Isotope ratios were calculated by averaging the isotopic ratios of each sweep in the analysis, and subsequently normalising to the NIST SRM 610 primary RM to correct for matrix independent instrument mass bias and drift. Samples with ^{175}Lu count rates < 4.81 Mcps were calibrated to NIST SRM 610 ratios measured in pulse mode and above this value, the Lu/Hf ratios were calibrated to NIST SRM 610 ratios in analogue mode (Glorie *et al.* 2024). The following isotopes were measured ('+' refers to mass-shifted isotopes), with dwell times in milliseconds between brackets: ^{27}Al(2), ^{43}Ca(2), $^{47+66}$Ti(2), ^{53}Cr(2), ^{55}Mn(2), ^{57}Fe(2), ^{88}Sr(2), $^{89+83}$Y(2), $^{90+83}$Zr(2), $^{140+15}$Ce(2), ^{146}Nd(2), ^{147}Sm(2), ^{172}Yb(5), ^{175}Lu(10), $^{175+82}$Lu(100), $^{176+82}$Hf(200), $^{178+82}$Hf(150). Titanium, Sr, Zr, Ce and Yb signals were monitored for inclusions of titanite/rutile, apatite, zircon, monazite and xenotime, respectively. Given down-hole fractionation is not observed in the applied Lu-Hf method (Simpson *et al.* 2021), no down-hole fractionation corrections were applied.

The Lu-Hf ages were calculated using inverse isochron regression (Li and Vermeesch 2021) in IsoplotR (Vermeesch 2018), based on the matrix-corrected ^{176}Lu/^{176}Hf and ^{177}Hf/^{176}Hf isotopic ratios, their 2SE uncertainties, the calculated error correlations, and the decay constant after Scherer *et al.* (2001) and Söderlund *et al.* (2004). Reported uncertainties are within 95% confidence intervals. Lu-Hf ages are presented both before and after calibration for laser-induced elemental fractionation, with the latter being calibrated to Högsbo garnet (Simpson *et al.* 2021, 2023, Glorie *et al.* 2024). For the calibrated Lu-Hf ages, the uncertainty on the measured Högsbo inverse isochron age was propagated to each sample in quadrature. BP-1 garnet (monazite U-Pb reference age of 1745 ± 14 Ma) and Heftjetjern garnet (multi-session garnet Lu-Hf isochron age of 930.3 ± 1.4 Ma) were measured as secondary RM (Simpson *et al.* 2023, Glorie *et al.* 2024). Matrix-corrected against Högsbo garnet data yielded an inverse isochron age of 1746 ± 8 Ma (N = 32, MSWD = 1.3) for BP-1, and 930 ± 2 Ma (N = 24, MSWD = 1.1) for Heftjetjern garnet.

Error propagation

Error propagation should consider the random uncertainties (analytical uncertainties derived from counting statistics, RM calibration and drift), as well as systematic uncertainties derived from matrix-matched correction and the long-term (multi-session) variance of isotope ratios (i.e., intra-session reproducibility) (Horstwood *et al.* 2016). The propagated analytical uncertainties are calculated within both Iolite and LADR, and inter-session reproducibility has recently been demonstrated to be relatively small (~ 0.1% relative standard deviation; Glorie *et al.* 2024), the uncertainty on the matrix-matching correction needs to be included to provide a minimum estimate of the total age uncertainty. The relative uncertainty of the $^{176}Lu/^{177}Hf$ ages of the matrix-matched RM should be quadratically propagated to the sample isochron age uncertainties for each session (Equation 1):

$$\text{Total age uncertainty} = \sqrt{\text{Sample age uncertainty}^2(\%) + \text{RM age uncertainty}^2_{\text{Laser}}(\%) + \text{RM age uncertainty}^2_{\text{ID}}(\%)} \quad (1)$$

Results

Garnet microstructures, major and trace elements

Garnet GWA-1 grains are mostly subhedral, containing small zircon, quartz and apatite inclusions, and are commonly crosscut by sets of random fractures across the whole grain (Figure 3a). GWA-1 lacks evidence of widespread intracrystalline deformation as indicated by the low textural misorientation map (Figure 3a), with domains of increased relative misorientation associated with fractures and cracks (Figure 3b). GWA-2 is mostly euhedral and inclusion- and fracture-free, also lacking evidence of crystal-plastic deformation in the textural component map and profile (Figure 3c, d). In summary, neither GWA-1 nor GWA-2 show signs of crystal-plastic deformation.

X-ray elemental maps (represented in % *m/m*) of a ~ 1 mm diameter GWA-1 garnet indicate a diffuse chemical variability core and rim with a smooth decrease in Fe, Mn and increase in Ca, Mg from core to rim (Figure 4a). GWA-1 is dominated by almandine (X_{Alm} ~ 0.64–0.62; from core to rim) and grossular (X_{Grs} ~ 0.30–0.31), with minor pyrope (X_{Prp} ~ 0.02–0.01) and spessartine (X_{Sps} ~ 0.01) composition (Figure 4b). The major element zoning is interpreted to reflect intragrain diffusion during prograde metamorphism in response to Rayleigh fractionation (Caddick *et al.* 2010, Lanari and Engi 2017, Rubatto *et al.* 2020). The garnet core is depleted in Sc, V, Ga, Y, Yb and Lu relative to the rim and cracks (Figure 4c). The preservation of unmodified growth zoning suggests rapid cooling, consistent with the thermal evolution of the Albany-Fraser Orogen (Kirkland *et al.* 2011, Scibiorski *et al.* 2015, 2016), and unaffected by any subsequent high-temperature metamorphic overprint (> 650 °C) (Caddick *et al.* 2010). Lutetium mass fraction follows the zoning pattern of heavy rare earth elements (HREE), with variable mass fractions from ~ 2 μg g^{-1} in the core to ~ 15 μg g^{-1} in the rim. Hafnium mass fraction is very low across the whole garnet (below detection limit of a regular quadrupole instrument), with higher mass fraction along cracks up to ~ 1.5 μg g^{-1}. From these textural observations we infer a single garnet growth stage.

X-ray elemental maps of a ~ 1 mm diameter for GWA-2 indicate a diffuse texture between core and rim in the Fe-Mg-Mn maps, whereas the Ca map displays a sharp distinction between the inner core outer, core and rim zones (Figure 5a). The core is dominated by relatively high Fe-Mg contents, decreasing towards the garnet rim with concomitant increasing Ca-Mn contents. GWA-2 is composed of almandine (X_{Alm} ~ 0.58–0.50; from core to rim) and spessartine (X_{Sps} ~ 0.37–0.47), with low pyrope (X_{Prp} ~ 0.04–0.02) and negligible X_{Grs} contents (below 0.1) (Figure 5b). The diffuse core-rim transition and the X_{Alm}-X_{Sps}-X_{Prp} profile shapes may reflect intragrain diffusion during rapid cooling in response to Rayleigh fractionation (Caddick *et al.* 2010, Rubatto *et al.* 2020). Trace element maps of GWA-2 display great complexity between cores and rims (Figure 5c). The garnet core shows well-defined oscillatory zoning with comparatively lower Y, Zr and Lu contents and higher V and Ga. The core-rim transition is defined by a sharp increase in Y, Zr and Lu. Anomalous regions with high Ti and Zr in the inner-core are also evident, and Ti, Y, Zr and Lu concentrated in well-defined domains parallel to the core-rim boundary akin to asymmetric quarter mats microstructures. Lutetium mass fraction varies from core (~ 1.0 μg g^{-1}) to rim (~ 12.0 μg g^{-1}), with significantly higher mass fraction (up to ~ 25 μg g^{-1}) in quarter mats microstructures. The transition core-rim is depleted in Hf (below detection limit of a regular quadrupole), with Hf up to ~ 1.0 μg g^{-1} in the rim. Although the major element zoning, especially Fe-Mg-Mn, imply a single garnet growth stage, the trace element zoning highlights chemical complexity in

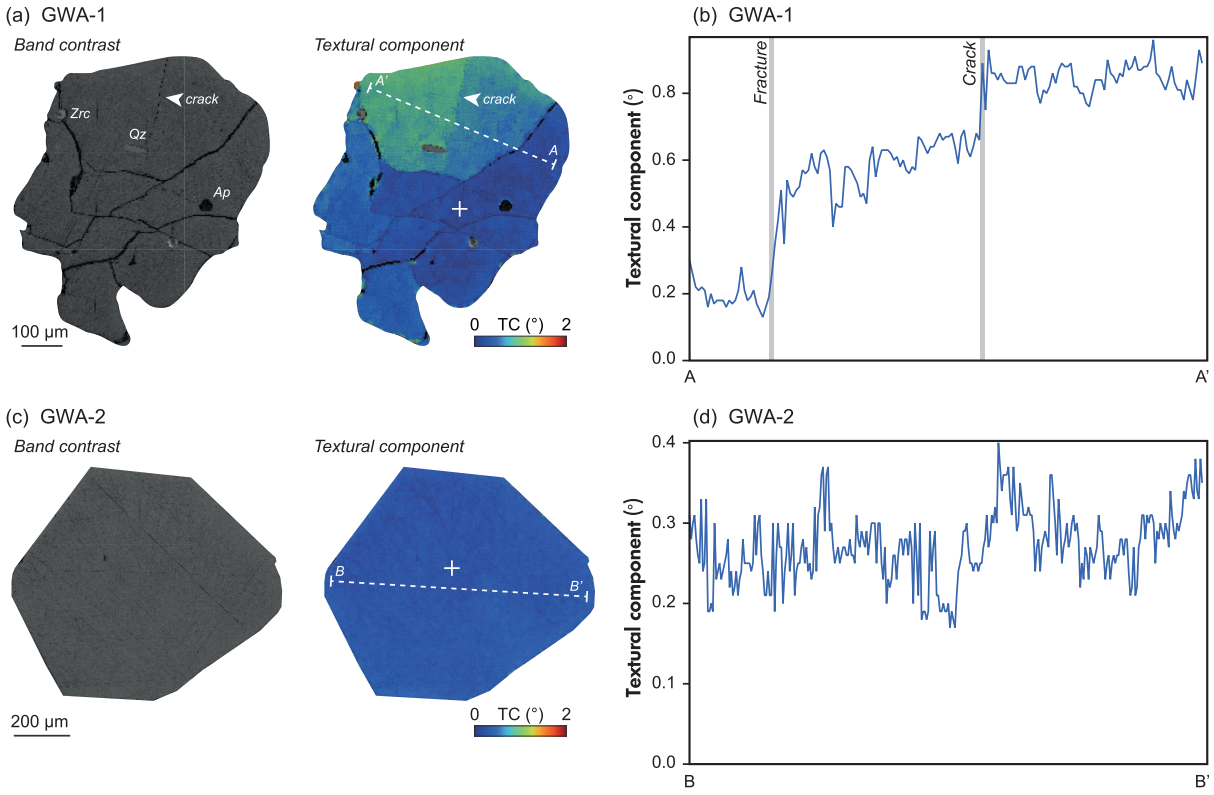

Figure 3. Band contrast and textural component maps (relative to the white-cross reference) and associated textural component profiles across GWA-1 (A–A') and GWA-2 (B–B').

this garnet growth processes involving rare earth element supply and uptake during magmatic evolution (e.g., Devoir *et al.* 2021).

Solution ID Lu-Hf geochronology

The ID Lu-Hf measurements in GWA-1 indicate bulk garnet Lu and Hf mass fractions are between 6.09–7.75 µg g^{-1} and 1.03–2.98 µg g^{-1}, respectively. The isotopic ratios obtained for the three GWA-1 aliquots, along with the whole-rock fraction, yielded a Lu-Hf isochron age of 1267.0 ± 3.0 Ma (MSWD = 1.5) and an initial $^{176}Hf/^{177}Hf_i$ of 0.281415 ± 0.000012 (Figure 6a). This garnet age is consistent with cooling after Albany-Fraser Orogen Stage I (Clark *et al.* 2000, Kirkland *et al.* 2011), and with the youngest zircon grains within this sample (Figure 2a).

GWA-2 yielded bulk garnet Lu and Hf mass fractions between 8.48–8.68 µg g^{-1} and 0.22–1.69 µg g^{-1}, respectively. Three GWA-2 aliquots and the whole-rock fraction yielded a garnet Lu-Hf isochron age of 934.7 ± 1.4 Ma (MSWD = 1.7) and $^{176}Hf/^{177}Hf_i$ of 0.281386 ± 0.000013 (Figure 6b), consistent with the zircon crystallisation age of 938 ± 4 Ma (Figure 2a). These ages reflect the formation of pegmatite bodies in the Capricorn Orogen in response to the Kuparr tectonic event (955–830 Ma) (Olierook *et al.* 2019).

In situ Lu-Hf geochronology

For the Curtin dataset, GWA-1 Lu-Hf data from session one yield an uncorrected (i.e., calibrated against NIST SRM 610 only, and not calibrated for laser-induced matrix dependant elemental fractionation) inverse isochron age of 1317 ± 32 Ma (2.4% uncertainty) and $^{176}Hf/^{177}Hf_i$ of 0.2803 ± 0.0095 (N = 42, MSWD = 0.9, Figure 7a), with a positive offset of 4.0% from the ID Lu-Hf age. The results from session two define an uncorrected inverse isochron age of 1381 ± 26 Ma (1.9% uncertainty) and $^{176}Hf/^{177}Hf_i$ of 0.2802 ± 0.0061 (N = 42, MSWD = 0.9, Figure 7b), with age positive offset of 9.0% compared with the ID Lu-Hf. The Lu-Hf data from session three yield an uncorrected inverse isochron age of 1257 ± 18 Ma (1.4% uncertainty) and $^{176}Hf/^{177}Hf_i$ of 0.2768 ± 0.0069 (N = 47, MSWD = 1.2, Figure 7c), showing an age offset of -0.8% and demonstrating good fit with the ID Lu-Hf isochron age considering

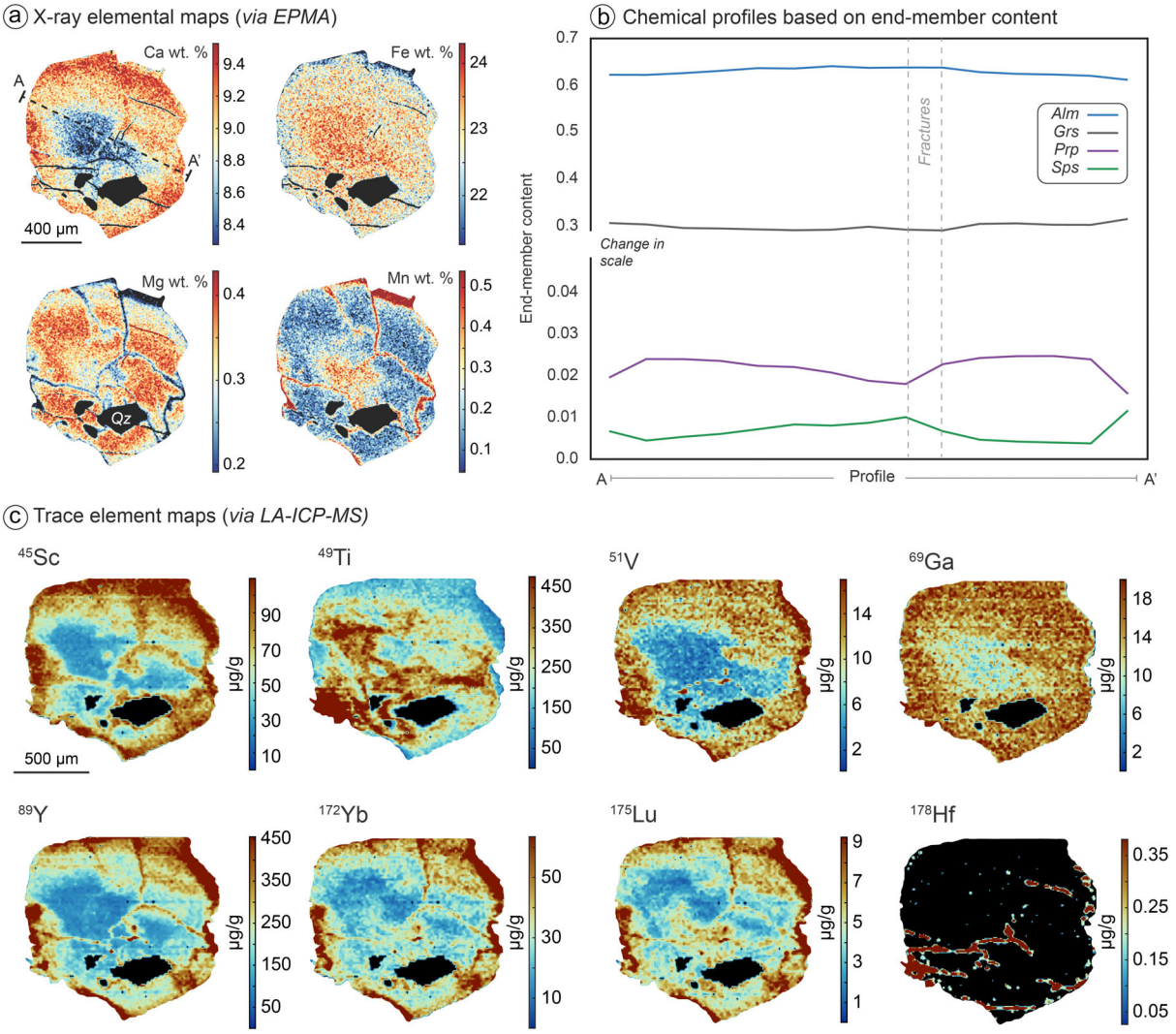

Figure 4. Chemical and microstructural characterisation of GWA-1. (a) X-ray elemental maps; (b) Chemical profile (A–A′) based on the garnet end-members content; (c) Trace element maps.

uncertainties. The GWA-1 data collected at the University of Adelaide yield an uncorrected inverse isochron age of 1314 ± 15 Ma (1.1% uncertainty) and $^{176}Hf/^{177}Hf_i$ of 0.2827 ± 0.0013 (N = 38, MSWD = 1.3, Figure 7d), indicating a positive offset of 3.7% from the ID Lu-Hf age.

For the Curtin dataset, GWA-2 Lu-Hf data from session one yield an uncorrected inverse isochron age of 973 ± 28 Ma (3.0% uncertainty) and $^{176}Hf/^{177}Hf_i$ of 0.2869 ± 0.0082 (N = 43, MSWD = 0.7, Figure 8a), and positive age offset of 4.0%. The results from session two define an uncorrected inverse isochron age of 1029 ± 25 Ma (uncertainty of 2.4%) and $^{176}Hf/^{177}Hf_i$ of 0.2793 ± 0.0035 (N = 44, MSWD = 1.1, Figure 8b), indicating positive age offset of 10% from the ID Lu-Hf age. Session three yield an uncorrected inverse isochron age 940 ± 14 Ma (1.5% uncertainty) and $^{176}Hf/^{177}Hf_i$ of 0.2822 ± 0.0022 (N = 48, MSWD = 1.1, Figure 8c), and positive age offset of 0.5% indicating good agreement with the ID Lu-Hf isochron age considering uncertainties. The data collected at the University of Adelaide yield an uncorrected inverse isochron age of 965 ± 12 Ma and (1.3% uncertainty) $^{176}Hf/^{177}Hf_i$ of 0.2869 ± 0.0029 (N = 44, MSWD = 0.9, Figure 8d), indicating an positive offset of 3.2%. We note that despite the core-rim distinct Lu-Hf mass fractions and trace element pattern, all *in situ* Lu-Hf data defined statistically robust single isochrons, demonstrating that both textural domains are in isotopic equilibrium.

In summary, GWA-1 and GWA-2 results consistently yield older inverse isochron ages with an offset up to 10% (depending on analytical conditions) compared with the ID

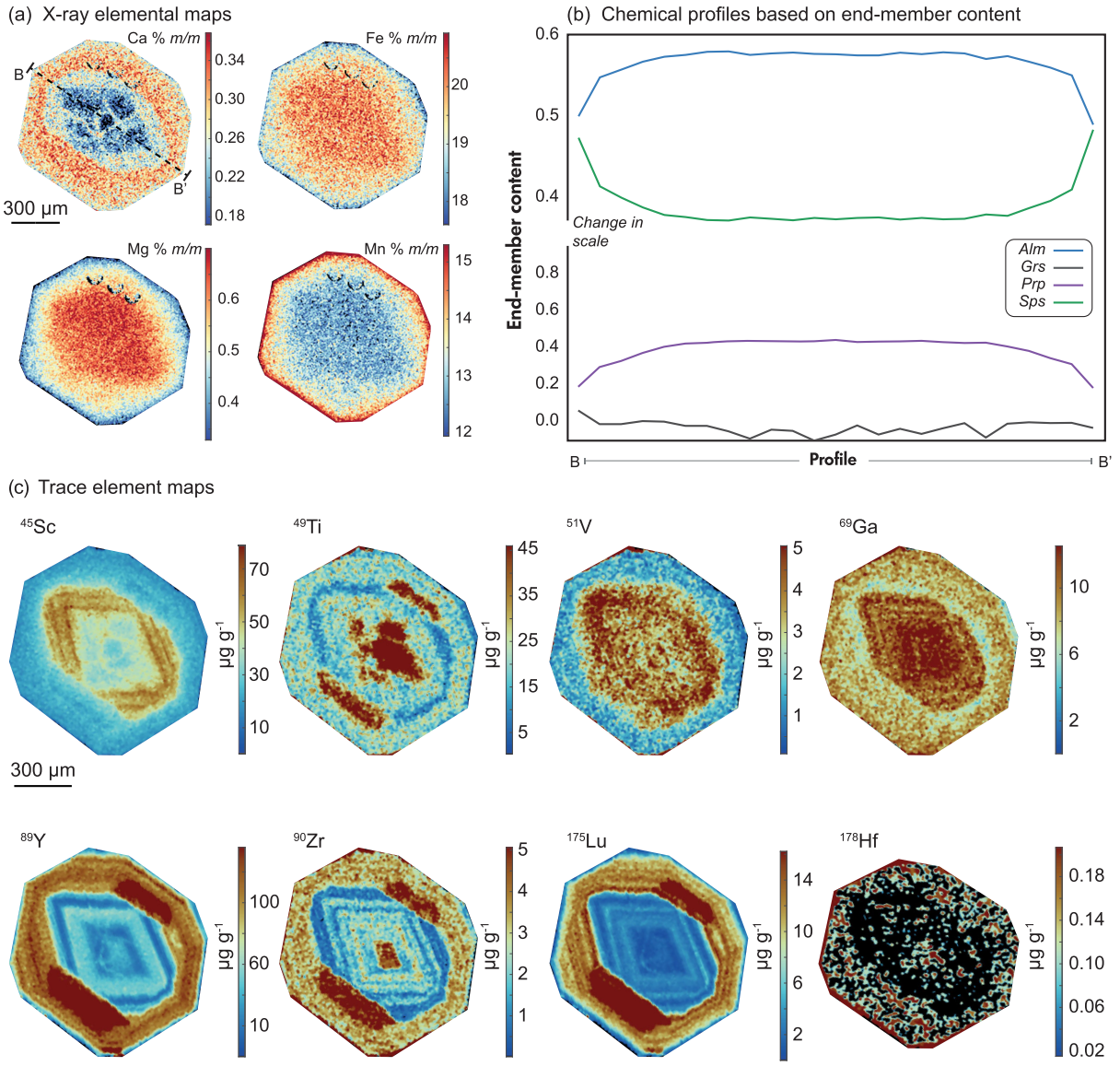

Figure 5. Chemical and microstructural characterisation of GWA-2. (a) X-ray elemental maps; (b) Chemical profile (B–B′) based on the garnet end-members content; (c) Trace element maps.

Lu-Hf crystallisation age, with uncertainties below 3.0% and achieving a best uncertainty of ~1.1%. Nevertheless, we note that both RMs present similar age offsets within the same session, suggesting that the offset is predictable and correctable (Simpson *et al.* 2021).

Discussion

Matrix and analytical effects

Isochron age offsets for *in situ* Lu-Hf geochronology have been attributed to matrix effects arising from differences in ablation characteristics between garnet samples and the NIST SRM 610 calibration glass (Simpson *et al.* 2021). Our results reveal isochron age offsets up to 10% that are variable between sessions, but consistent for GWA-1 and GWA-2 when both RMs are analysed in the same measurement session. This age offset consistency allows the use of characterised RMs to correct for such effect. Notably, the ages obtained in Curtin sessions two and three display contrasting offsets of 9–10% and ~0.5%, respectively. Such different results indicate that variations in ICP-MS tuning conditions lead to differences in mass bias (e.g., instrumental mass fractionation), as laser-induced matrix effects can be expected to produce consistent magnitudes of offsets across multiple analytical

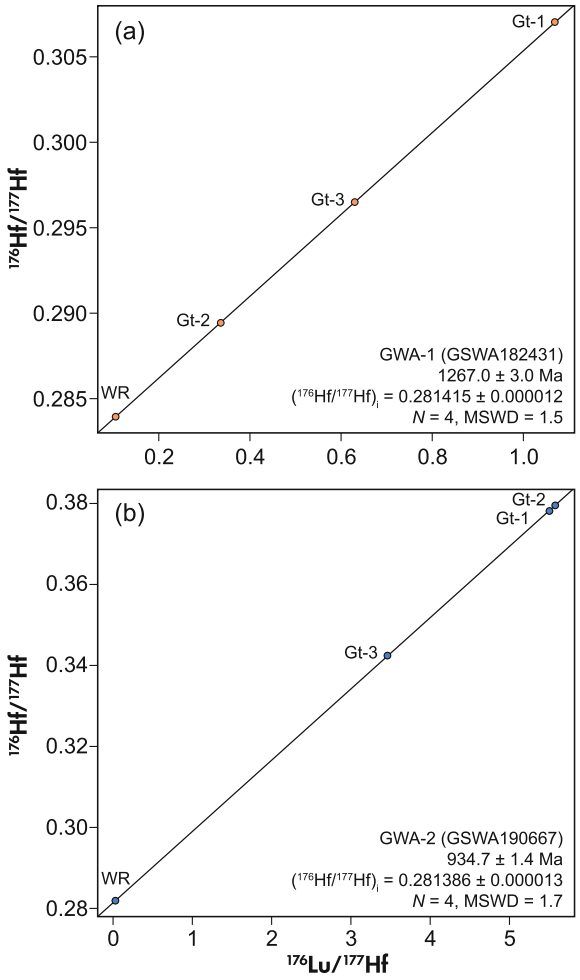

Figure 6. Lu-Hf isochrons of garnets (a) GWA-1 and (b) GWA-2 from solution ID Lu-Hf isotopic measurement. Ages and uncertainties are stated at the 95% level of confidence. Data symbols are larger than the analytical uncertainties for visualisation purposes.

sessions in the same material, with the same analytical conditions (Ireland 2004).

Aside from small differences in lenses settings (omega bias and lens, Q1 entrance and cell entrance) mostly affecting gross relative mass sensitivity, the main tuning differences between sessions two and three are in the octopole bias and energy discrimination applied to the reaction cell (Table 1). Our results indicate that the significant octopole bias (-3.1 V) and energy discrimination (-20 V) used in session two likely induced mass bias favouring the heavier isotopes (e.g., ^{178}Hf over ^{176}Hf). This inference is supported by the difference in mass bias (^{178}Hf/^{176}Hf ratio of 5.26 for session two, and 5.21 for session three) measured in reference glass NIST SRM 610, with results from session two being significantly higher than the natural ^{178}Hf/^{176}Hf isotopic abundance (~ 5.20). Thus, we conclude that aside from laser-induced matrix effects, instrument tuning conditions may also contribute to differences in age offsets, either positive or negative.

In order to obtain reliable *in situ* garnet Lu-Hf isochron ages, it is necessary to apply a matrix correction factor (MC_f) to the ^{176}Lu/^{176}Hf ratio (per analysis) based on the behaviour of garnet reference materials with known references ages determined through ID Lu-Hf (e.g., GWA-1 and GWA-2). The MC_f is calculated based on the uncorrected isochron age (Unc_{age}, My) and the reference age from ID Lu-Hf (Ref_{age}, My), taking into consideration the ^{176}Lu decay constant (λ, My^{-1}) after Söderlund *et al.* (2004) (Equation 2). The inverse isochron ages recalculated using the matrix corrected ^{176}Lu/^{176}Hf ratios are taken as reliable.

$$MC_f = \frac{^{176}Lu}{^{176}Hf} * \left[\frac{e^{Unc_{age}*\lambda}-1}{e^{Ref_{age}*\lambda}-1}\right] \quad (2)$$

We cross-calibrated GWA-1 and GWA-2 to test their suitability as RMs to account for matrix correction and assess secondary age reproducibility. When using the age offset observed in GWA-2 as a correction factor (session specific), GWA-1 yielded corrected inverse isochron ages consistent with the crystallisation age for each analytical session and laboratory (Figure 9a). Similarly, GWA-2 yields inverse isochron ages consistent with crystallisation age when corrected against GWA-1 (session specific factor) (Figure 9b). Irrespective of the reason for such age offsets, this cross-calibration confirms that both RMs can account for matrix and instrument effects and can accurately provide an independent secondary age accuracy check. Previously, *in situ* garnet Lu-Hf ratios have been matrix-corrected against Högsbo garnet considering the columbite U-Pb age as the inferred garnet Lu-Hf age (Simpson *et al.* 2021), and other RMs such as BP-1 and Heftjetjern with multi-session reference ages (Simpson *et al.* 2023, Glorie *et al.* 2024) were employed for secondary age check. We assess the reliability of GWA garnet by correcting known RMs (Högsbo, BP-1 and Heftjetjern) against GWA-2. The Högsbo garnet yields an inverse isochron age of 1022 ± 3 Ma (N = 20, MSWD = 1.5), and the BP-1 and Heftjetjern garnet yield inverse isochron ages of 1734 ± 8 Ma (N = 34, MSWD = 1.3) and 923 ± 2 Ma (N = 24, MSWD = 1.1), respectively. These ages agree with reference multi-session ages for such RMs considering propagated uncertainties (Simpson *et al.* 2023, Glorie *et al.* 2024), reinforcing that GWA garnet

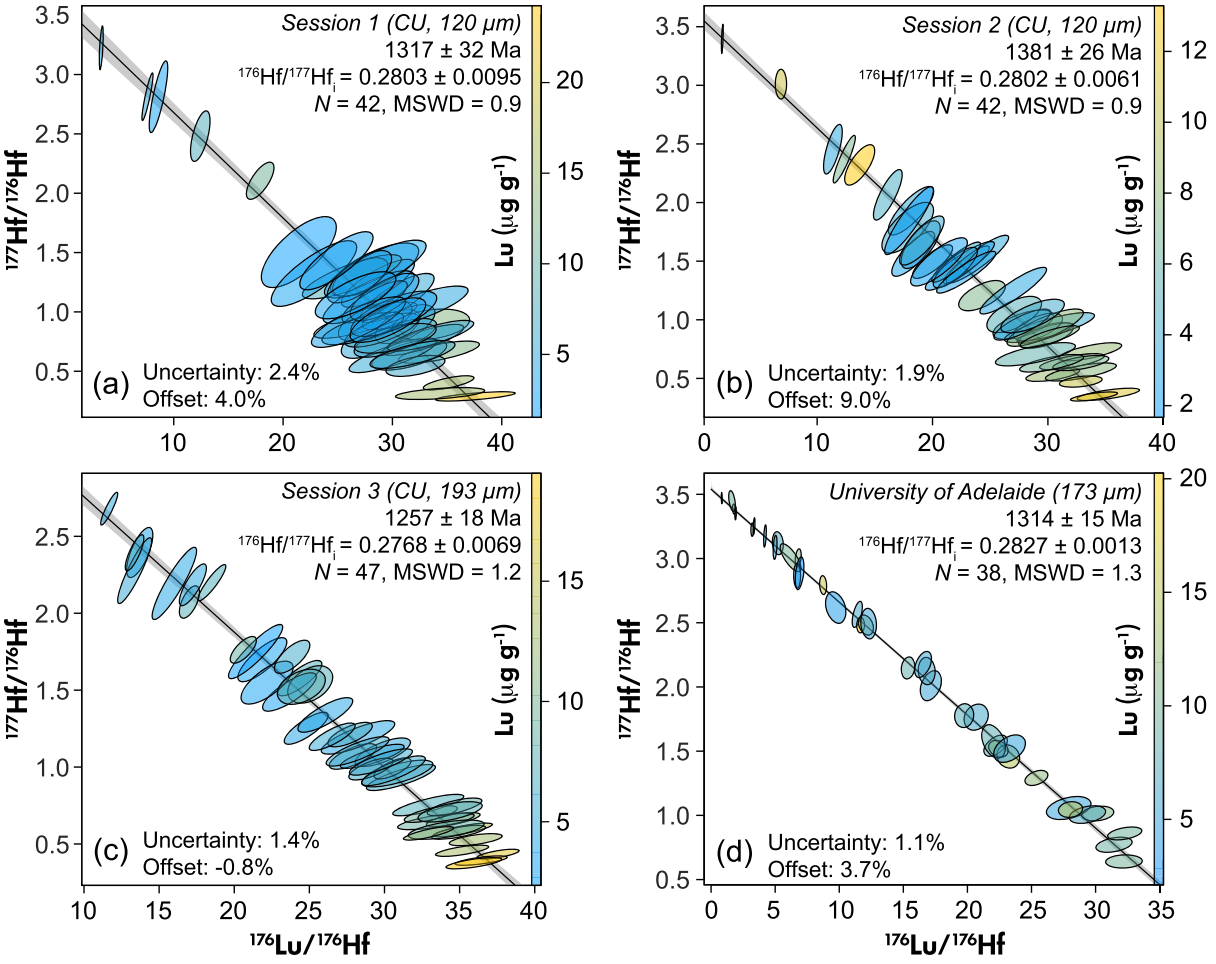

Figure 7. Inverse Lu-Hf isochrons of GWA-1 from *in situ* isotopic measurement of multi-grains. For discussion purposes, the Lu-Hf ratios have not been matrix corrected. Spot size is specified in the top right corner of each panel. Data presented in panels a–c were collected at Curtin University (CU), and those collected at the University of Adelaide are presented in panel d. Ages and uncertainties are stated at the 95% level of confidence.

presented here produce accurate and reliable data compared with independently published ages.

Importantly, we do not observe any relationship between matrix effects and the major element chemistry of GWA-1 (almandine-grossular-bearing) and GWA-2 (almandine-spessartine-bearing). This demonstrates a lack of end-member composition matrix effects.

Comparison of instrument sensitivity and analytical uncertainties

One of the critical factors for *in situ* Lu-Hf measurement is the sensitivity of the LA-ICP-MS/MS for accurately measuring mass-shifted Hf isotope ratios at the highest possible precision. To test different approaches and improve instrument sensitivity, distinct reaction cell flushing approaches were undertaken for the data collected at Curtin University (see section *In situ Lu-Hf geochronology – Curtin University*). To evaluate the influence of flushing the reaction cell with high NH_3/He flow rate prior to analysis, we converted the ^{175}Lu and ^{178}Hf count rates from the reference glass NIST SRM 610 to be equivalent to 50 µm (smallest spot size used) to compare equal ablation volumes. Session one was conducted without flushing the reaction cell prior to analysis, yielding mean ^{175}Lu and ^{178}Hf count rates of $\sim 2 \times 10^6$ and $\sim 3 \times 10^5$ counts per second (cps), respectively (Figure 10a, b). Sessions two and three were carried out after flushing the reaction cell with high NH_3/He for 0.5 h and 2.0 h, yielding mean ^{175}Lu count rates of $\sim 3.8 \times 10^6$ and $\sim 4.1 \times 10^6$ cps (Figure 10a), and mean

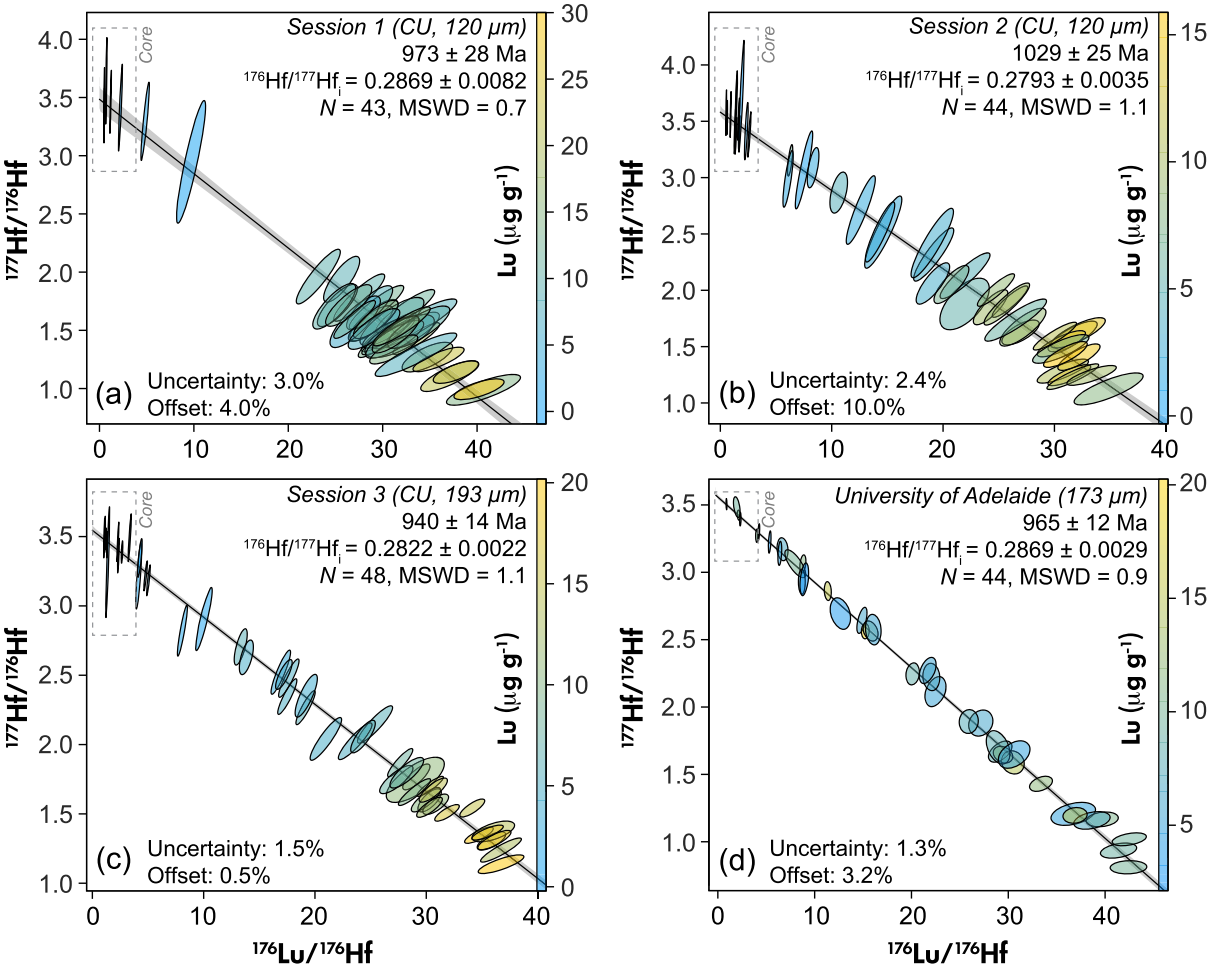

Figure 8. Inverse Lu-Hf isochrons of GWA-2 from *in situ* isotopic measurement of multi-grains. For discussion purposes, the Lu-Hf ratios have not been matrix corrected. Specific spot size is specified in the top right corner of each panel. Data presented in panels a–c were collected at Curtin University (CU), and those collected at the University of Adelaide are presented in panel d. Ages and uncertainties are stated at the 95% level of confidence.

^{178}Hf count rates of $\sim 5 \times 10^5$ and $\sim 6 \times 10^5$ cps (Figure 10b), respectively. These results indicate an increase in ^{175}Lu count rates of ~22% (session two) and ~32% (session three) compared with session one. Since ^{175}Lu is mostly unreactive to NH_3, the increase in Lu sensitivity likely reflects instrument tuning changes affecting gross relative mass sensitivity. However, ^{178}Hf count rates increase in ~70% for 0.5 h cell flush (session two), and ~100% for 2.0 h cell flush compared with session one. Although the increase might have been influenced by small instrumental differences, such a large magnitude increase in count rates is unlikely to be related to the instrument settings alone. We posit that flushing the reaction cell promotes an increase in the reaction efficiency and conversion rate (^{178}Hf ➔ $^{178+82}$Hf). This increase in instrument sensitivity lowered the GWA-1 ^{176}Lu/^{177}Hf measured ratio uncertainty (2*s*) from 9 to 4%, and the ^{176}Hf/^{177}Hf measured ratio uncertainty from 14 and 6% (Figure 10c). Similarly, the GWA-2 ^{176}Lu/^{177}Hf and ^{176}Hf/^{177}Hf measured ratio uncertainties were reduced from 5 to 2%, and from 9 to 4%, respectively. This substantial improvement in internal uncertainties improved the inverse isochron age uncertainty from ~3.0% (session one, no reaction cell flush) to 1.5% (session three, 2.0 h reaction cell flush). Thus, flushing the reaction cell with a high NH_3/He flow rate (> 90% in the mass flow controller #3) for at least 2 h, and tuning the instrument to maximise sensitivity, are recommended to improve reaction efficiency, which in turns reduces the uncertainty for geochronology applications. For comparison, the measurement session at Adelaide Microscopy (see section *In situ Lu-Hf geochronology – Curtin University*) was conducted after 4 h of reaction cell flushing at maximum gas flow rate. Mean count rates for ^{175}Lu and

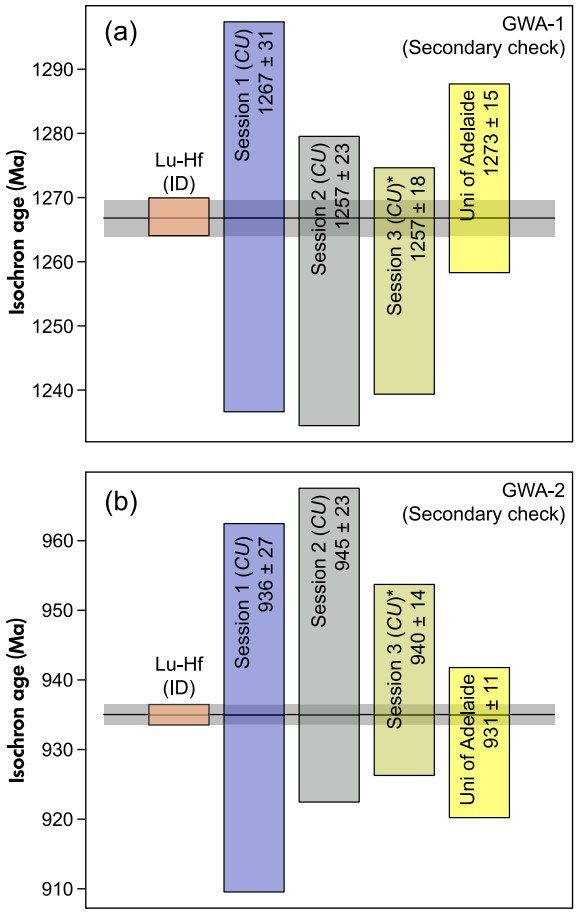

Figure 9. Normalised isochron ages of GWA-1 (a; corrected by GWA-2) and GWA-2 (b; corrected by GWA-1). (*) Isochron ages from session three were not corrected given that the age offset compared with the ID Lu-Hf age is smaller than the analytical uncertainty. Ages and uncertainties are stated at the 95% level of confidence.

^{178}Hf measured in NIST SRM 610 and converted to a comparable 50 μm spot size, were ~ 7×10^6 for ^{175}Lu and ~ 9×10^5 μm for ^{178}Hf.

Common-^{176}Hf component (R^{176})

Given the initial Hf composition has negligible influence on age determination for materials with variable Lu/Hf ratios and varies little over Earth history (Blichert-Toft and Albarède 1997, Bizzarro *et al.* 2003), two-point isochron dates between an assumed ^{177}Hf/^{176}Hf$_i$ and the measured ratios can be calculated for the garnet Lu-Hf system. In this context, we calculate the contribution of common-Hf (R^{176} [%]), assuming a simple two component radiogenic-common mixing array within single garnet Lu-Hf analysis. The common-Hf fraction is defined by the distance along the isochron between the initial ^{177}Hf/^{176}Hf ratio (mean ~ 3.55 ± 0.07) and the radiogenic component, in inverse space, calculated via Pythagoras theorem (Equation 3). This value provides a useful metric to judge the dependence of the calculated model age on the assumed initial ^{177}Hf/^{176}Hf ratio (i.e., low R^{176} data has lower age dependency on the ^{177}Hf/^{176}Hf$_i$, and vice versa). The R^{176} considers the ^{176}Lu decay constant (λ, My^{-1}) after Söderlund *et al.* (2004), measured ratios (*m*), ^{177}Hf/^{176}Hf$_i$ (anchored to 3.55 ± 0.07, Simpson *et al.* 2022) and the inverse isochron age (*t*, Ma).

$$R^{176}\,(\%) = \left(1 - \frac{\sqrt{\left(\frac{1}{e^{\lambda t}-1} - \left(\frac{^{176}Lu}{^{176}Hf}\right)_m\right)^2 + \left(\frac{^{177}Hf}{^{176}Hf}\right)_m^2}}{\sqrt{\left(\frac{1}{e^{\lambda t}-1}\right)^2 + \left(\frac{^{177}Hf}{^{176}Hf}\right)_i^2}}\right) * 100 \quad (3)$$

Based on the *in situ* Lu-Hf data from all sessions, the R^{176} index indicate a common-Hf component of GWA-1 between 8–90% with median of 31%, and 28–99% common-Hf for garnet GWA-2 with median of 63%. The comparatively lower common Hf component of GWA-1 is reflected in slightly better inverse isochron age uncertainties compared with GWA-2 (Figures 7 and 8).

Availability of garnet reference materials

At the time of publication of this paper, several 1-inch^2 polished mounts with approximately fifteen to twenty grains (Figure 11a) and additional garnet separates of GWA-1 and GWA-2 (~ 5 g each) are available for distributions across laboratories and research institutions. A substantial amount of rock from each garnet RM (~ 190 g for GWA-1, and ~ 160 g for GWA-2; Figure 11c) has been reserved for rock processing and mineral separation to maintain the future supply of such materials. Both garnet RMs are available for distribution upon contact with Dr Bruno Ribeiro via email (bruno.vieiraribeiro@curtin.edu.au).

Conclusions

In this paper, we demonstrated that almandine-grossular GWA-1 and almandine-spessartine GWA-2 can be employed as RMs for *in situ* garnet Lu-Hf geochronology via LA-ICP-MS/MS. The microstructural and chemical

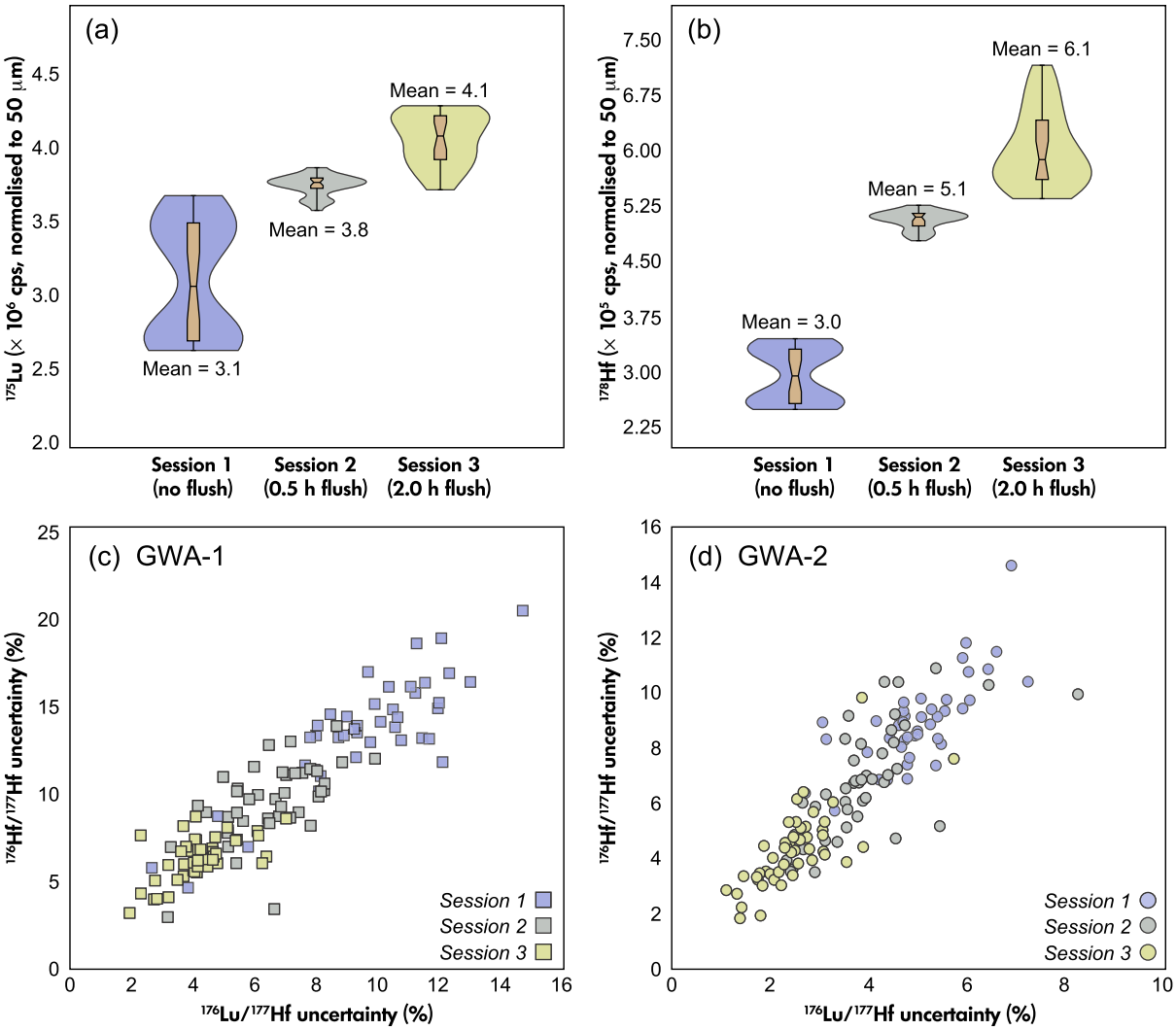

Figure 10. **^{175}Lu and ^{178}Hf count rates (counts per second [cps], a, b) and isotopic ratio uncertainties (c, d) in response to distinct collision cell flushing approaches with high $NH_{3(g)}$ flow rate prior to analysis. ^{175}Lu and ^{178}Hf count rates were measured on the reference glass NIST SRM 610 and normalised to 50-μm spot size to minimise sampling volume effects. Isotopic ratio uncertainties refer to garnets GWA-1 and GWA-2. Session 1: no flush, session 2: 0.5 h flush, session 3: 2.0 h flush.**

characterisation of these garnet indicates that they grew during a single growth event, consistent with their well-defined solution ID Lu-Hf isochrons for each material. Garnet GWA-1 yielded a Lu-Hf ID crystallisation age of 1267.0 ± 3.0 Ma with $^{176}Hf/^{177}Hf_i$ of 0.281415 ± 0.000012, and garnet GWA-2 yielded a Lu-Hf ID crystallisation age of 934.7 ± 1.4 Ma with $^{176}Hf/^{177}Hf_i$ of 0.281386 ± 0.000013. In both cases, the ID Lu-Hf age is interpreted to date the timing of closure to radiogenic Hf diffusion coeval with garnet crystallisation.

The *in situ* inverse isochrons Lu-Hf ages are systematically older than the ID crystallisation age, which we interpret is due to matrix effects between the NIST SRM 610 calibration RM and garnet, and to session specific instrumental tuning (ICP-MS/MS and reaction cell) conditions used to maximise sensitivity. Correcting for such effects is achieved by applying a session specific correction factor in the $^{176}Lu/^{176}Hf$ ratio for both GWA-1 and GWA-2, which behave similarly throughout each measurement session. Additional matrix effects associated with the garnet major element chemistry were not observed. GWA-1 and GWA-2 can yield inverse isochron ages with uncertainties as low as 1.1%, depending on instrument sensitivity, but a > 2 h high flow rate flushing of the reaction cell with NH_3/He is recommended prior to commencing analysis.

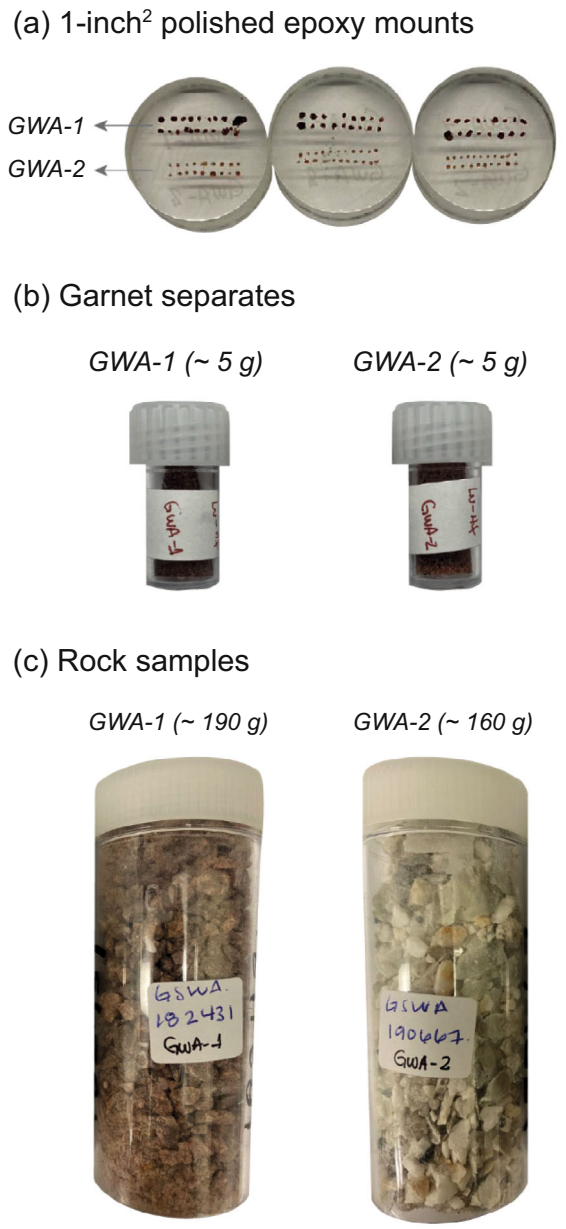

Figure 11. Garnet reference materials currently available (at the time of publication of this paper). (a) 1-inch² polished epoxy mounts; (b) garnet separate fractions with ~5 g of each material; (c) rock samples available for mineral separation (c). The polished mounts and the garnet separate fractions are available for distribution.

The well-characterised garnet GWA-1 and GWA-2 are suitable as secondary RMs for *in situ* garnet Lu-Hf geochronology to account for matrix effects and to enable accuracy checks on inverse isochron ages.

Acknowledgements

This study was financially supported by the Timescales of Mineral Systems Group (Curtin University), the Natural Sciences and Engineering Research Council of Canada (Discovery Grant RGPIN-2015-04080) and the Canadian Foundation of Innovation and the British Columbia Knowledge Development Fund (joint infrastructure grant 229814) to MAS. S. Glorie was supported by an Australian Research Council Future Fellowship (FT210100906). Research in the John de Laeter Centre GeoHistory laser ablation facility is enabled by AuScope (auscope.org.au) and the Australian Government via the National Collaborative Research Infrastructure Strategy (NCRIS). This research was undertaken using the Tescan Clara FESEM (ARC LE190100176). BVR acknowledge technical support from Fred Fryer (Agilent Technologies). The authors thank the Geological Survey of Western Australia for providing specimens of samples GSWA 182431 (GWA-1) and GSWA 190667 (GWA-2). FJK publishes with the permission of the Executive Director, Geological Survey of Western Australia. The authors are thankful for insightful comments from two anonymous reviewers, and for Paul Sylvester's editorial handling. Open access publishing facilitated by Curtin University, as part of the Wiley - Curtin University agreement via the Council of Australian University Librarians.

Scientific editing by Paul J. Sylvester.

Data availability statement

The data are available in the supplementary material of this paper.

References

Baxter E.F., Caddick M.J. and Dragovic B. (2017) Garnet: A rock-forming mineral petrochronometer. **Reviews in Mineralogy and Geochemistry, 83**, 469–533.

Baxter E.F. and Scherer E.E. (2013) Garnet geochronology: Timekeeper of tectonometamorphic processes. **Elements, 9**, 433–438.

Bizzarro M., Baker J.A., Haack H., Ulfbeck D. and Rosing M. (2003) Early history of Earth's crust-mantle system inferred from hafnium isotopes in chondrites. **Nature, 421**, 931–933.

Blichert-Toft J. and Albarède F. (1997) The Lu-Hf isotope geochemistry of chondrites and the evolution of the mantle-crust system. **Earth and Planetary Science Letters, 148**, 243–258.

references

Blichert-Toft J., Boyet M., Télouk P. and Albarède F. (2002)
^{147}Sm-^{143}Nd and ^{176}Lu-^{176}Hf in eucrites and the differentiation of the HED parent body. **Earth and Planetary Science Letters**, **204**, 167–181.

Brown M. and Johnson T. (2018)
Secular change in metamorphism and the onset of global plate tectonics. **American Mineralogist**, **103**, 181–196.

Caddick M.J., Konopásek J. and Thompson A.B. (2010)
Preservation of garnet growth zoning and the duration of prograde metamorphism. **Journal of Petrology**, **51**, 2327–2347.

Cawood P.A. (2020)
Metamorphic rocks and plate tectonics. **Science Bulletin (Beijing)**.

Cawood P.A., Chowdhury P., Mulder J.A., Hawkesworth C.J., Capitanio F.A., Gunawardana P.M. and Nebel O. (2022)
Secular evolution of continents and the Earth system. **Reviews of Geophysics**, **60**, https://doi.org/10.1029/2022RG000789

Cawood P.A., Hawkesworth C.J. and Dhuime B. (2013)
The continental record and the generation of continental crust. **Geological Society of America Bulletin**, **125**, 14–32.

Clark D.J., Hensen B.J. and Kinny P.D. (2000)
Geochronological constraints for a two-stage history of the Albany-Fraser Orogen, Western Australia. **Precambrian Research**, **102**, 155–183.

Devoir A., Bloch E. and Müntener O. (2021)
Residence time of igneous garnet in Si-rich magmatic systems: Insights from diffusion modeling of major and trace elements. **Earth and Planetary Science Letters**, **560**, 116771.

Gaidies F., Mccarron T., Simpson A.D., Easton R.M., Glorie S., Putlitz B. and Trebus K. (2023)
Polymetamorphism during the Grenvillian Orogeny in SE Ontario: Results from trace element mapping, *in situ* geochronology, and diffusion geospeedometry. **Journal of Metamorphic Geology**, **42**, 35–61.

Glorie S., Simpson A., Gilbert S.E., Hand M. and Müller A.B. (2024)
Testing the reproducibility of *in situ* Lu Hf dating using Lu-rich garnet from the Tørdal pegmatites, southern Norway. **Chemical Geology**, 122038.

Gordon S.M., Kirkland C.L., Reddy S.M., Blatchford H.J., Whitney D.L., Teyssier C., Evans N.J. and McDonald B.J. (2021)
Deformation-enhanced recrystallization of titanite drives decoupling between U-Pb and trace elements. **Earth and Planetary Science Letters**, **560**, 116810.

GSWA (2022)
1:10 000 000 Simplified tectonic map of Western Australia. **Geological Survey of Western Australia (Perth, Western Australia)**.

Holder R.M., Viete D.R., Brown M. and Johnson T.E. (2019)
Metamorphism and the evolution of place tectonics. **Nature**, **572**, 378–381.

Horstwood M.S.A., Košler J., Gehrels G., Jackson S.E., McLean N.M., Paton C., Pearson N.J., Sircombe K., Sylvester P., Vermeesch P., Bowring J.F. and Condon D.J. and Schoene B. (2016)
Community-derived standards for LA-ICP-MS U-(Th-)Pb geochronology – Uncertainty propagation, age interpretation and data reporting. **Geostandards and Geoanalytical Research**, **40**, 311–332.

Hu Z., Gao S., Liu Y., Hu S., Chen H. and Yuan H. (2008)
Signal enhancement in laser ablation ICP-MS by addition of nitrogen in the central channel gas. **Journal of Analytical Atomic Spectrometry**, **23**, 1093.

Ireland T.R. (2004)
SIMS Measurement of stable isotopes. **Handbook of stable isotope analytical techniques. Elsevier**, 652–691.

Kaempf J., Johnson T.E., Clark C., Alfing J., Brown M., Lanari P. and Rankenburg K. (2024)
Paleoarchean metamorphism in the Acasta Gneiss Complex: Constraints from phase equilibrium modelling and *in situ* garnet Lu-Hf geochronology. **Journal of Metamorphic Geology**, **42**, 373–394.

Kirkland C.L., Spaggiari C.V., Pawley M.J., Wingate M.T.D., Smithies R.H., Howard H.M., Tyler I.M., Belousova E.A. and Poujol M. (2011)
On the edge: U-Pb, Lu-Hf, and Sm-Nd data suggests reworking of the Yilgarn craton margin during formation of the Albany-Fraser Orogen. **Precambrian Research**, **187**, 223–247.

Lanari P. and Engi M. (2017)
Local bulk composition effects on metamorphic mineral assemblages. **Reviews in Mineralogy and Geochemistry**, **83**, 55–102.

Lanari P., Vidal O., De Andrade V., Dubacq B., Lewin E., Grosch E.G. and Schwartz S. (2014)
XMapTools: A MATLAB©-based program for electron microprobe X-ray image processing and geothermobarometry. **Computers and Geosciences**, **62**, 227–240.

Li Y. and Vermeesch P. (2021)
Inverse isochron regression for Re-Os, K-Ca and other chronometers. **Geochronology preprint**. https://doi.org/10.5194/gchron-2021-7

May W., Parris R., Beck C., Fassett J., Greenberg R., Guenther F. and Kramer G. (2000)
Definitions of terms and modes used at NIST for value-assignment of reference materials for chemical measurements. **NIST Special Publication**, **260**, 136pp.

references

Millonig L.J., Albert R., Gerdes A., Avigad D. and Dietsch C. (2020)
Exploring laser ablation U-Pb dating of regional metamorphic garnet – The Straits Schist, Connecticut, USA. Earth and Planetary Science Letters, 552, 116589.

Mulder J.A., Nebel O., Gardiner N.J., Cawood P.A., Wainwright A.N. and Ivanic T.J. (2021)
Crustal rejuvenation stabilised Earth's first cratons. Nature Communications, 12, 3535.

Münker C., Weyer S., Scherer E. and Mezger K. (2001)
Separation of high field-strength elements (Nb, Ta, Zr, Hf) and Lu from rock samples for MC-ICP-MS measurements. Geochemistry, Geophysics, Geosystems, 2, https://doi.org/10.1029/2001GC000183

Nebel O., Morel M.L.A. and Vroon P.Z. (2009)
Isotope dilution determinations of Lu, Hf, Zr, Ta and W, and Hf isotope compositions of NIST SRM 610 and 612 glass wafers. Geostandards and Geoanalytical Research, 33, 487–499.

Norris A. and Danyushevsky L. (2018)
Towards estimating the complete uncertainty budget of quantified results measured by LA-ICP-MS. Abstract. Goldschmidt Conference (Boston, MA, USA).

Olierook H.K.H., Agangi A., Plavsa D., Reddy S.M., Yao W., Clark C., Occhipinti S.A. and Kylander-Clark A.R.C. (2019)
Neoproterozoic hydrothermal activity in the West Australian Craton related to Rodinia assembly or breakup? Gondwana Research, 68, 1–12.

Palin R.M., Santosh M., Cao W., Li S.-S., Hernández-Uribe D. and Parsons A. (2020)
Secular change and the onset of plate tectonics on Earth. Earth-Science Reviews, 207, 103172.

Papapavlou K., Darling J.R., Storey C.D., Lightfoot P.C., Moser D.E. and Lasalle S. (2017)
Dating shear zones with plastically deformed titanite: New insights into the orogenic evolution of the Sudbury impact structure (Ontario, Canada). Precambrian Research, 291, 220–235.

Piechocka A.M., Gregory C.J., Zi J.-W., Sheppard S., Wingate M.T.D. and Rasmussen B. (2017)
Monazite trumps zircon: Applying SHRIMP U-Pb geochronology to systematically evaluate emplacement ages of leucocratic, low-temperature granites in a complex Precambrian orogen. Contributions to Mineralogy and Petrology, 172, 63.

Pollington A.D. and Baxter E.F. (2010)
High resolution Sm-Nd garnet geochronology reveals the uneven pace of tectonometamorphic processes. Earth and Planetary Science Letters, 293, 63–71.

Reddy S.M., Timms N.E., Hamilton P.J. and Smyth H.R. (2009)
Deformation-related microstructures in magmatic zircon and implications for diffusion. Contributions to Mineralogy and Petrology, 157, 231–244.

Reddy S.M., Timms N.E., Pantleon W. and Trimby P. (2007)
Quantitative characterization of plastic deformation of zircon and geological implications. Contributions to Mineralogy and Petrology, 153, 625–645.

Ribeiro B.V., Finch M.A., Cawood P.A., Faleiros F.M., Murphy T.D., Simpson A., Glorie S., Tedeschi M., Armit R. and Barrote V.R. (2022)
From microanalysis to supercontinents: Insights from the Rio Apa Terrane into the Mesoproterozoic SW Amazonian Craton evolution during Rodinia assembly. Journal of Metamorphic Geology, 40, 631–663.

Ribeiro B.V., Lagoeiro L., Faleiros F.M., Hunter N.J.R., Queiroga G., Raveggi M., Cawood P.A., Finch M. and Campanha G.A.C. (2020)
Strain localization and fluid-assisted deformation in apatite and its influence on trace elements and U-Pb systematics. Earth and Planetary Science Letters, 545, 116421.

Ribeiro B. V., Kirkland C.L., Kelsey D.E., Reddy S.M., Hartnady M.I.H., Faleiros F.M., Rankenburg K., Liebmann J., Korhonen F.J. and Clark C. (2023)
Time-strain evolution of shear zones from petrographically constrained Rb-Sr muscovite analysis. Earth and Planetary Science Letters, 602, 117969.

Rubatto D., Burger M., Lanari P., Hattendorf B., Schwarz G., Neff C., Keresztes Schmidt P., Hermann J., Vho A. and Günther D. (2020)
Identification of growth mechanisms in metamorphic garnet by high-resolution trace element mapping with LA-ICP-TOFMS. Contributions to Mineralogy and Petrology, 175, 61.

Scherer E., Münker C. and Mezger K. (2001)
Calibration of the lutetium-hafnium clock. Science (1979) 293, 683–687.

Scibiorski E., Tohver E. and Jourdan F. (2015)
Rapid cooling and exhumation in the western part of the Mesoproterozoic Albany-Fraser Orogen, Western Australia. Precambrian Research, 265, 232–248.

Scibiorski E., Tohver E., Jourdan F., Kirkland C.L. and Spaggiari C. (2016)
Cooling and exhumation along the curved Albany-Fraser orogen, Western Australia. Lithosphere, 8, 551–563.

Seman S., Stockli D.F. and McLean N.M. (2017)
U-Pb geochronology of grossular-andradite garnet. Chemical Geology, 460, 106–116.

Shu Q., Beranoaguirre A., Albert R., Millonig L.J., Walters J.B., Marschall H.R., Gerdes A., Hoefer H.E., Hezel D. and Brey G.P. (2024)
Multi-stage ultrahigh temperature metamorphism in the lower crust of the Kaapvaal craton recorded by U-Pb ages of garnet. Contributions to Mineralogy and Petrology, 179, 49.

Simpson A., Gilbert S., Tamblyn R., Hand M., Spandler C., Gillespie J., Nixon A. and Glorie S. (2021)
In-situ Lu-Hf geochronology of garnet, apatite and xenotime by LA-ICP-MS/MS. Chemical Geology, 577, 120299.

references

Simpson A., Glorie S., Hand M., Spandler C. and Gilbert S. (2023)
Garnet Lu-Hf speed dating: A novel method to rapidly resolve polymetamorphic histories. **Gondwana Research**, 121, 215–234.

Simpson A., Glorie S., Hand M., Spandler C., Gilbert S. and Cave B. (2022)
In situ Lu-Hf geochronology of calcite. **Geochronology**, 4, 353–372.

Slama J., Košler J., Condon D.J., Crowley J.L., Gerdes A., Hanchar J.M. Horstwood M.S.A., Morris G.A., Nasdala L., Norberg N., Schaltegger U., Schoene B., Tubrett M.N. and Whitehouse M.J. (2008)
Plesovice zircon – A New natural reference material for U-Pb and Hf isotopic microanalysis. **Chemical Geology**, 249, 1–35.

Smit M.A., Ratschbacher L., Kooijman E. and Stearns M.A. (2014)
Early evolution of the Pamir deep crust from Lu-Hf and U-Pb geochronology and garnet thermometry. **Geology**, 42, 1047–1050.

Smit M.A., Scherer E.E. and Mezger K. (2013)
Lu-Hf and Sm-Nd garnet geochronology: Chronometric closure and implications for dating petrological processes. **Earth and Planetary Science Letters**, 381, 222–233.

Söderlund U., Patchett P.J., Vervoort J.D. and Isachsen C.E. (2004)
The ^{176}Lu decay constant determined by Lu-Hf and U-Pb isotope systematics of Precambrian mafic intrusions. **Earth and Planetary Science Letters**, 219, 311–324.

Spaggiari C.V., Kirkland C.L., Smithies R.H. and Wingate M.T.D. (2014)
Tectonic links between Proterozoic sedimentary cycles, basin formation and magmatism in the Albany-Fraser Orogen, Western Australia. **Geological Survey of Western Australia Report**, 133, 63pp.

Spencer C.J. (2022)
Biogeodynamics: Coupled evolution of the biosphere, atmosphere, and lithosphere. **Geology**, 50, 867–868.

Spencer C.J., Davies N.S., Gernon T.M., Wang X., McMahon W.J., Morrell T.R.I., Hincks T., Pufahl P.K., Brasier A., Seraine M. and Lu G.-M. (2022)
Composition of continental crust altered by the emergence of land plants. **Nature Geoscience**, 15, 735–740.

Sprung P., Scherer E.E., Upadhyay D., Leya I. and Mezger K. (2010)
Non-nucleosynthetic heterogeneity in non-radiogenic stable Hf isotopes: Implications for early solar system chronology. **Earth and Planetary Science Letters**, 295, 1–11.

Tamblyn R., Hand M., Simpson A., Gilbert S., Wade B. and Glorie S. (2021)
In situ laser ablation Lu-Hf geochronology of garnet across the Western Gneiss Region: Campaign-style dating of metamorphism. **Journal of the Geological Society of London**, jgs2021-94.

Timms N.E., Kinny P.D., Reddy S.M., Evans K., Clark C. and Healy D. (2011)
Relationship among titanium, rare earth elements, U-Pb ages and deformation microstructures in zircon: Implications for Ti-in-zircon thermometry. **Chemical Geology**, 280, 33–46.

Tual L., Smit M.A., Cutts J., Kooijman E., Kielman-Schmitt M., Majka J. and Foulds I. (2022)
Rapid, paced metamorphism of blueschists (Syros, Greece) from laser-based zoned Lu-Hf garnet chronology and LA-ICP-MS trace element mapping. **Chemical Geology**, 607, 121003.

Vermeesch P. (2018)
IsoplotR: A free and open toolbox for geochronology. **Geoscience Frontiers**, 9, 1479–1493.

Vervoort J.D. and Blichert-Toft J. 1999)
Evolution of the depleted mantle: Hf isotope evidence from juvenile rocks through time. **Geochimica et Cosmochimica Acta**, 63, 533–556.

Vervoort J.D., Patchett P.J., Söderlund U. and Baker M. (2004)
Isotopic composition of Yb and the determination of Lu concentrations and Lu/Hf ratios by isotope dilution using MC-ICP-MS. **Geochemistry, Geophysics, Geosystems**, 5, https://doi.org/10.1029/2004GC000721

Walters J.B. (2022)
MinPlot: A mineral formula recalculation and plotting program for electron probe microanalysis. **Mineralogia**, 53, 51–66.

Wiedenbeck M., Allé P., Corfu F., Griffin W.L., Meier M., Oberli F., von Quadt A., Roddick J.C. and Spiegel W. (1995)
Three natural zircon standards for U-Th-Pb, Lu-Hf, trace element and REE analyses. **Geostandards Newsletter**, 19, 1–23.

Wingate M.T.D., Kirkland C.L. and Johnson S.P. (2011)
190667: Granite pegmatite, Camel Hill. **Geochronology Record 1003: Geological Survey of Western Australia**, 6pp.

Wingate M.T.D., Lu Y., Kirkland C.L. and Spaggiari C.V. (2016)
182431: Psammitic gneiss, Gwynne Creek. **Geochronology Record 1319: Geological Survey of Western Australia**, 6pp.

Wu S., Wang H., Yang Y., Niu J., Lan Z., Zhang L., Huang C., Xie L., Xu L., Yang J. and Wu F. (2023)
In situ Lu-Hf geochronology with LA-ICP-MS/MS analysis. **Journal of Analytical Atomic Spectrometry**, 38, 1285–1300.

GEOSTANDARDS and GEOANALYTICAL RESEARCH

Supporting information

The following supporting information may be found in the online version of this article:

Appendix S1. Electron probe microanalyser measurement results.

Appendix S2. Lu-Hf *in situ* isotope measurement results for garnets GWA-1 and -2.

This material is available from: http://onlinelibrary.wiley.com/doi/10.1111/ggr.12579/abstract (This link will take you to the article abstract).